Cement and Concrete Research 189 (2025) 107735

Contents lists available at ScienceDirect

Cement and Concrete Research

journal homepage: www.elsevier.com/locate/cemconres

Basic creep properties of hydrates in mature slag-based CEM II concretes: A micromechanical analysis

Maximilian Sorgner [a], Rodrigo Díaz Flores [a], Bernhard Pichler [a], Thomas Pilgerstorfer [b], Bernd Moritz [c], Christian Hellmich [a,*]

[a] Institute for Mechanics of Materials and Structures, TU Wien (Vienna University of Technology), Karlsplatz 13/202, 1040 Vienna, Austria
[b] Geoconsult ZT GmbH, Urstein Süd, 5412 Puch bei Hallein, Austria
[c] ÖBB-Infrastruktur AG, Streckenmanagement und Anlagenentwicklung, Fachbereich Bautechnik-Tunnelbau, Europaplatz 12/1, 8020 Graz, Austria

ARTICLE INFO

Keywords:
Slag-based CEM II hydrates
Basic creep
Micromechanics
Aging creep
Long-term creep

ABSTRACT

The demand for accurate characterization of slag-based CEM II concretes is becoming increasingly important as the construction sector shifts towards eco-efficient materials. Here, the basic creep behavior of slag-based CEM II concretes is traced back to mixture-invariant hydrate properties. Therefore, an experimentally validated three-step micro-viscoelastic model for CEM I/OPC-concretes is complemented by a Powers-Acker-type hydration model for CEM II and extended towards long-term creep, temperature activation, and moisture sensitivity. This model is used for a strain rate-based, aging viscoelastic analysis of two creep tests on distinctively different CEM II concretes; revealing that the shear creep modulus of CEM II hydrates is half as large as the one of ordinary Portland cement hydrates. This makes slag-based CEM II concretes especially suitable for applications such as precast segmental tunnel linings, where a faster stress relaxation under displacement-controlled conditions is beneficial.

1. Introduction

Motivated by the desire to reduce the environmental impact of cement production, cement mixtures with supplementary cementitious materials, such as silica fume, fly ash, and ground granulated blast-furnace slag, are frequently used in concrete engineering [1,2]. For general construction purposes, CEM II has, in recent decades, enjoyed an increased popularity as a more ecological alternative to ordinary Portland cement (OPC, also referred to as CEM I). CEM II is a mixture of OPC and additives with a mass content of up to 35% [3]. These additives, including fly ash, slag, or limestone, may have a significant effect on the material properties of the respective concrete mixtures, motivating extensive research activities [4,5].

In the present contribution, we set the corresponding focus on basic creep properties, and how they are influenced by the slag content. In this context, it is particularly interesting to compare concrete systems with the same water-to-binder and aggregate-to-binder ratios, but being based on CEM I and slag-based CEM II, respectively. As a result, increasing the mass of added slag, while reducing the Portland cement content by the same mass percentage, has been shown to yield increased creep strains, over creep testing times between 150 and 500 days [6,7]. These results were corroborated by micromechanical short-term creep tests on cement paste, where cantilever beam-type samples with square cross sections of $300\,\mu\text{m} \times 300\,\mu\text{m}$ were loaded over holding times ranging from one to one thousand seconds [8]. Herein, we go a step further and target the creep properties of the hydrates arising from a slag-based CEM II material, in comparison to hydrates forming in traditional Portland cement mixes.

For this purpose, we resort to a micromechanical approach, which has turned out as very helpful in the context of OPC-based concretes [9–12], and introduce two modeling-related innovations: (i) The classical Powers-Acker hydration model, developed for CEM I, is adapted to consider the reaction of clinker and slag with water, and to provide a relation between the hydration degree and the volume fractions of the constituents making up the material system; (ii) the micromechanical model described in [9,11] is extended towards thermal, moisture, and aging effects, covering both short-term as well as long-term creep of concrete. In more detail, we break down the material into aggregates, unhydrated cement constituents, cement hydrates, and water; and downscale the basic creep behavior of two different slag-based mature CEM II concretes to the viscoelasticity of hydrates arising from CEM II. The viscoelastic behavior of CEM II hydrates can then be compared to the known creep behavior of CEM I hydrates, so as to give a yet more profound and quantitative answer to the question on basic differences between CEM I and CEM II material systems.

---

* Corresponding author.
E-mail address: christian.hellmich@tuwien.ac.at (C. Hellmich).

https://doi.org/10.1016/j.cemconres.2024.107735
Received 28 June 2024; Received in revised form 24 September 2024; Accepted 18 November 2024

This strategy is closely related to pertinent work documented in the open scientific literature: The classical approach for upscaling linear viscoelastic properties from the microstructural scale of a composite to the overall composite properties is the correspondence principle [13, 14]: It allows to transform the involved Boltzmann integro-differential equations into a series of formally elastic problems in the Laplace–Carson space, which can then be treated with classical homogenization methods of continuum micromechanics, such as Mori–Tanaka or self-consistent methods [15]. However, things become more intricate with concrete, a material undergoing aging. When restricting the resolution of the material to a cement paste matrix with aggregate inclusions, then the matrix itself does not exhibit any more a linear viscoelastic, but an aging viscoelastic behavior. This requires significant modifications of the classical correspondence principle-based homogenization strategies, with respective solutions being based either on the age-adjusted effective modulus method together with the transformation field analysis [16], or on a Volterra integral operator-based method [17]. If, in addition, the impact of complex aggregate shapes on the creep properties is of interest, then numerical simulations are the preferred choice [18,19]. Once the cement paste itself is resolved into yet smaller micromechanical material phases, such as unhydrated clinker, unhydrated supplementary cementitious materials, water, and hydration products, then additional theoretical challenges come up, arising from the evolving, time-dependent volume fractions of the aforementioned material phases. In order to adapt the aforementioned homogenization approach even for this situation, Sanahuja and Huang [20] came up with the interesting proposition to introduce, within an RVE of cement paste, very many "fictitious" phases with formally non-aging creep functions representing pore-to-solid and solid-to-solid transformations mimicking the hydration process. While delivering qualitatively plausible results, the approach was "(quote from [20]) illustrated on a representation of cement paste, which is too simplified to allow a quantitative comparison of aging creep functions to experimental results (end quote)". On the other hand, an alternative approach to the problem of creep of hydrating concrete, proposed by Scheiner and Hellmich [21], did undergo experimental validation. There, the use of the correspondence principle was restricted to single time points, for which integro-differential equations for strain rates, rather than for strains, were formulated [21]. Respective creep rate functions are retrieved from time-derivation of classically homogenized non-aging creep functions used only at one time point with the associated invariant microstructure. This approach proved very useful in the context of tunnel safety assessment, via various types of structural mechanics models [22–25], and it is also used in the present paper. Moreover, the use of homogenization theory to downscale mechanical properties of concrete or cement paste down to the properties of hydrates is repeatedly documented in the literature [9,26–28]. Such a downscaling approach is the key to the investigations reported in the present paper.

The latter is organized as follows: In Section 2, experimental investigations on slag-based CEM II concrete, including nanoindentation tests as well as macroscopic creep tests performed on two different types of CEM II concretes [29,30], are summarized. In order to identify the maturity of the tested concretes, a microelastic model for concrete made from slag-based CEM II is introduced in Section 3, and it allows us to identify the evolution of the hydration degree of concrete over the time of creep testing. Thereafter, in Section 4, the model is extended to consider thermally activated, moisture sensitive, short-to-long term aging viscoelasticity, so as to allow for downscaling the creep test results collected at tunnel construction site KAT3 [29], down to the shear creep modulus of slag-based CEM II hydrates. The resulting creep compliance is validated against independent, additional creep test data, namely those provided by Dummer et al. [30]. The results are discussed in Section 5, followed by conclusions in Section 6.

Table 1
Isotropic elastic stiffness properties of the solid constituents of slag-based CEM II concrete: bulk modulus k_i and shear modulus μ_i; note: pores do not exhibit a solid stiffness: $k_{por} = \mu_{por} = 0\,\text{GPa}$.

Constituent		k_i [GPa]	μ_i [GPa]	Ref.
clinker	$i = cli$	116.7	53.8	[26,31]
slag	$i = slg$	56.1	42.1	[36]
hydrates	$i = hyd$	18.7	11.8	[26,33,38]
limestone	$i = lim$	32.6	17.2	[41]
dolomite	$i = dol$	33.3	22.4	[41]
granite	$i = grt$	21.6	14.2	[41]
quarzite	$i = qzt$	24.6	21.6	[41]
basalt	$i = blt$	41.7	28.7	[41]
diabase	$i = dbs$	45.6	32.1	[41]

2. Review of nanoindentation and macroscopic creep tests

2.1. *Micro-elasticity of concrete constituents*

As regards OPC, nanoindentation tests provided access to the mixture-independent elastic properties of clinker [31–33] and to the "averaged" elastic properties of the different types of "hydration products" in OPC (such as portlandite, ettringite, and calcium silicate hydrates) [33,34]. In more detail, one of the plane surfaces of cylindrical specimens with a diameter of 11.5 mm and a thickness of 10–15 mm was repeatedly indented up to a depth of 300–500 nm [32], which provided the material properties associated with a representative volume element measuring at most 150–250 nm [35,36]. The latter properties were also retrieved from flexural and torsional resonance frequency tests on prismatic thin-slab specimens with dimensions of 15 mm × 80 mm × 1 mm, made from nearly fully hydrated cement pastes with an initial water-to-cement mass ratio amounting to 0.42 [26,37], see "clinker" and "hydrates" in Table 1. Things are somewhat different when it comes to slag-based CEM II, a mixture of OPC clinker and slag: On the one hand, the mass densities of slag and clinker differ, and so do their elastic properties [26,36]. The latter have been quantified by means of nanoindentation tests on ultra-smoothed surfaces of cubic specimens made from hardened alkali-activated slag-fly ash mixes [36], see "clinker" and "slag" in Table 1. In more detail, surfaces measuring 10 mm × 10 mm were indented up to a depth of 60 nm, revealing the properties of RVEs measuring at most some 30 nm [35,36]. On the other hand, nanoindentation tests on cubic specimens with dimensions of 25 mm×25 mm×25 mm and with an indentation depth up to 375 nm [38], together with proton nuclear magnetic resonance (^{1}H NMR) tests [39], have shown that the micro-elastic behavior and the mass densities of hydrates made from a combination of clinker and slag are nearly identical to those made from clinker only [38,40]. Accordingly, even if the chemical composition of hydrates resulting from the reactions of combinations of clinker and slag with water is slightly different from those of OPC, their elastic behavior is very similar [26,38], see "hydrates" in Table 1. This table also reports elastic properties of commonly used aggregates [41].

2.2. *Macroscopic creep tests of KAT3 [29]*

An experimental campaign was devoted to the determination of the creep and shrinkage properties of the tubbing concrete used at construction lot KAT3 of Koralm tunnel [29]. This concrete was produced from CEM II/A-S 52.5 N and is characterized by a 28-day uniaxial compressive strength of $f_{c,28\text{d}} = 59.5\,\text{MPa}$, a 144-day elastic Young's modulus of $E_{con,144\text{d}} = 37.8\,\text{GPa}$, prevailing at the start of the creep test [29], and by the mixture given in Table 2. There, "A-S" refers to a Portland composite cement with a clinker mass fraction of 0.80–0.94 and a slag (S) mass fraction of 0.06–0.20 (as indicated by the letter "A"). "52.5" refers to the strength (in MPa) which is reached by a standard mortar 28 days after mixing, and "N" stands for normal (rather

Table 2
Mixture characteristics of concrete used at KAT3 construction lot [29].

Initial mass ratios	
water-to-clinker	$m_{\mathrm{H_2O}}/m_{cli} = 0.51$
slag-to-clinker	$m_{slg}/m_{cli} = 0.15$
limestone-to-clinker	$m_{lim}/m_{cli} = 0$
Initial apparent mass densities per volume of concrete	
CEM II/A-S 52.5 N	$\rho^{con}_{cemII}(\xi = 0) = 0.371\,\mathrm{g/cm^3}$
water	$\rho^{con}_{\mathrm{H_2O}}(\xi = 0) = 0.165\,\mathrm{g/cm^3}$
Composition of aggregates	
dolomite	$m_{dol}/m_{agg} = 0.276 \approx f^{agg}_{dol}$
limestone	$m_{lim}/m_{agg} = 0.276 \approx f^{agg}_{lim}$
granite	$m_{grt}/m_{agg} = 0.133 \approx f^{agg}_{grt}$
quarzite	$m_{qzt}/m_{agg} = 0.112 \approx f^{agg}_{qzt}$
basalt	$m_{blt}/m_{agg} = 0.104 \approx f^{agg}_{blt}$
diabase	$m_{dbs}/m_{agg} = 0.099 \approx f^{agg}_{dbs}$

Table 3
Stress levels, as well as temperature and humidity conditions of the creep tests reported in [29,30].

	KAT3 [29]	Dummer et al. [30]
Stress level	10 MPa	6.2–9.6 MPa
Temperature	21°C	20°C
Relative humidity	72%	97%

than rapid) early-age strength evolution. This implies an initial slag-to-clinker mass ratio $m_{slg}/m_{cli}(\xi = 0)$ ranging from 0.06 to 0.25, with an average value of 0.15, see Table 2.

Six concrete prisms with cross-sectional dimensions of 35 cm × 35 cm and a height of 70 cm were produced. The square prismatic (rather than cylindrical) shape was chosen in agreement with the Austrian standard ÖNORM B 4710-3 [42]. The cross-sectional dimensions allowed for an almost full-face load application by means of the available testing equipment. The ratio of two between the height and the length of the square edge allowed for the realization of a close-to-perfect *uniaxial* compressive stress state at the center of the specimens, where the strain gauges were embedded, i.e., a stress state virtually free from shear stresses resulting from friction in the interfaces between the load platens and the specimens, for more details see e.g. Appendix A of [43]. The strain gauges had a measurement length of 15 cm, and they reported the axial strains of the prismatic samples, from one day after production on. Roughly one week after production, the formworks were stripped off, and the prisms were exposed to the ambient air of the production hall, where they were stored right next to the tubbings. Before the start of the creep tests, all specimens were transferred into the Koralm tunnel, where the relative humidity was virtually constant throughout testing ($\varphi = 72 \pm 3\%$). During creep testing, the temperature inside the specimens was $T = 21 \pm 2$°C, see Table 3.

Three prisms were kept free of external loading throughout the entire measurement period covering 500 days. Strains recorded on these prisms qualify as shrinkage strains. 144 days after production, the other three prisms were subjected to a compressive axial force of 1235 kN, resulting in a permanent compressive normal stress amounting to $\sigma_{\exp} = -10\,\mathrm{MPa}$. Strains recorded on the prisms subjected to such an axial force qualify as creep strains. The ratio of the applied stress over the 28-day strength of the material amounts to only 16.8%, which indicates linear creep behavior. Hence, cracking events remain negligible [44]. The data acquisition system failed during two time periods, the first of which lasted for ten days, from day 361 to day 371 after production, and the second of which lasted for 42 days, from day 415 to day 457 after production.

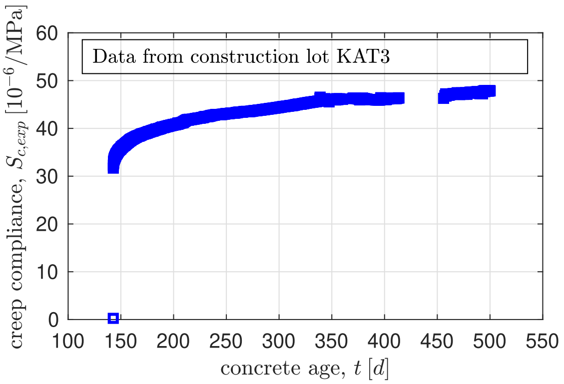

Fig. 1. Creep of concrete under uniaxial compression: creep compliance obtained from creep tests performed at KAT3 [29].

The total strains measured inside the compressed prisms comprise mechanical loading-induced basic creep strains (including instantaneous elastic strains and delayed viscoelastic strains), as well as load-independent autogeneous shrinkage and thermal strains. Hence, the basic creep strains were quantified by subtracting the strains measured in the load-free prisms from the strains measured in the compressed prisms. This was realized in terms of mean values computed from the data associated with the aforementioned test triples. In this context, we note that the data gained from different shrinkage or creep tests varied only marginally, which underlines the high level of repeatability attained during the experimental campaign.

In the following, the measured creep strains are normalized with respect to the applied stress, yielding the creep compliance $S_{\exp}(t-\tau)$, as

$$S_{\exp}(t-\tau) = \frac{\varepsilon_{\exp}(t-\tau)}{\sigma_{\exp}}\,, \qquad t \geq \tau\,, \tag{1}$$

where $\varepsilon_{\exp}$ refers to the mean value of the basic creep strains, t stands for the recording time starting from the time instant of concrete production, and τ stands for the time instant when the permanent compressive stress was subjected to the sample, see Fig. 1.

2.3. Macroscopic creep tests of Dummer et al. [30]

Dummer et al. performed creep experiments on concrete produced from CEM II/AM (S-L) 42.5 N, which is characterized by a 28-day uniaxial compressive strength of $f_{c,28\mathrm{d}} = 31.8 \pm 1.1\,\mathrm{MPa}$ and a 28-day elastic Young's modulus of $E_{con,28\mathrm{d}} = 30.3 \pm 0.26\,\mathrm{GPa}$, as well as by the mixture given in Table 4. Thereby, "AM (S-L)" refers to a Portland composite cement with a clinker mass fraction of 0.80–0.88 and with a slag (S)/limestone (L) mixture making up 12%–20% of the overall mass of the Portland composite cement. "42.5" refers to the strength (in MPa) which is reached by a standard mortar 28 days after mixing, and "N" refers to normal early-age strength evolution. Assuming equal masses of slag and limestone in the mixture, this results in an average slag-to-clinker mass ratio of 0.10, and in an average limestone-to-clinker mass ratio of 0.10, see Table 4.

Five cylindrical specimens with a diameter of 100 mm and a height of 300 mm were produced for performing basic creep tests under moderate compressive load, i.e., not exceeding one third of the sample's strength, $\sigma \leq 0.3\, f_{c,28\mathrm{d}}$. After 7 days of aging, the specimens were drilled out from a cube with an edge length of 310 mm. The dimension of the cube strongly suggest full water saturation of the samples. In order to prevent moisture release, they were sealed with four layers of plastic film covered by one layer of bitumen-coated aluminium foil. Due to self-desiccation, the relative humidity inside the specimens decreases by approximately 3% during the first 28 days ($\varphi = 97\%$) [45]. The specimens were stored in a climate chamber with a virtually constant temperature of $T = 20 \pm 1$°C, see Table 3. At an age of 28 days, the specimens were subjected to a constant compressive load, for a time span of 56 days. From simultaneous creep and shrinkage testing on these specimens, the mean value as well as the standard deviation of the creep compliance were obtained, see Fig. 2.

Table 4
Mixture characteristics of concrete investigated by Dummer et al. [30].

Initial mass ratios	
water-to-clinker	$m_{H_2O}/m_{cli} = 0.52$
slag-to-clinker	$m_{slg}/m_{cli} = 0.10$
limestone-to-clinker	$m_{lim}/m_{cli} = 0.10$
Initial apparent mass densities per volume of concrete	
CEM II/AM (S-L) 42.5 N	$\rho^{con}_{cemII}(\xi = 0) = 0.375\,\mathrm{g/cm^3}$
water	$\rho^{con}_{H_2O}(\xi = 0) = 0.165\,\mathrm{g/cm^3}$
Composition of aggregates	
dolomite	$m_{dol}/m_{agg} = 0 \approx f^{agg}_{dol}$
limestone	$m_{lim}/m_{agg} = 1 \approx f^{agg}_{lim}$
granite	$m_{grt}/m_{agg} = 0 \approx f^{agg}_{grt}$
quarzite	$m_{qzt}/m_{agg} = 0 \approx f^{agg}_{qzt}$
basalt	$m_{blt}/m_{agg} = 0 \approx f^{agg}_{blt}$
diabase	$m_{dbs}/m_{agg} = 0 \approx f^{agg}_{dbs}$

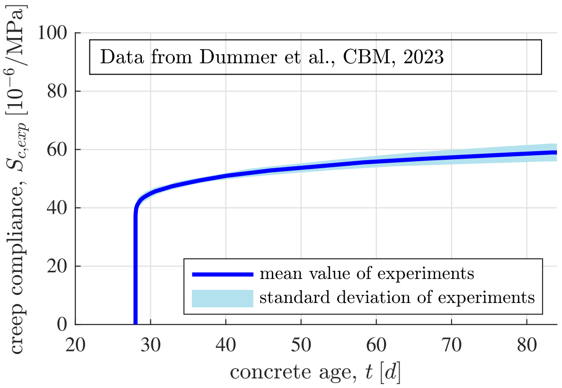

Fig. 2. Creep of concrete under uniaxial compression: creep compliance obtained from Dummer et al. [30].

3. Identification of hydration degree, via multiscale elastic modeling

3.1. Fundamentals of continuum micromechanics: Separation of scales principle

In continuum micromechanics [15], a macroscopically infinitesimal material volume is simultaneously considered as a micro-heterogeneous finite body that fills a representative volume element (RVE) with a characteristic length denoted as ℓ. This consideration requires fulfillment of the scale separation condition, reading as [15,46]

$$d \ll \ell \ll D\,, \tag{2}$$

where d stands for the characteristic length of inhomogeneities within the RVE and D stands for the characteristic length of the dimension or loading of a structure built from the material defined on the RVE. It is important to note that the first inequality ($\ll$) in Eq. (2) typically refers to a factor of 2 to 3 as concerns spherical heterogeneities [47], and to a factor of 4 as concerns non-flexible fibrous heterogeneities [48,49], while ℓ and D is typically separated by a factor of 5 to 50 [50].

In general, it is not possible to describe the microstructure within an RVE in full detail. Therefore, the description of the microstructure is reduced to the identification of key features, in terms of quasi-homogeneous subdomains called material phases. Accordingly, the mechanical behavior of the overall material is determined from the mechanical properties of these material phases, their shapes, their volume fractions, and their interactions. This is realized by combining phase-specific material behavior, such as linear elasticity or viscoelasticity, with averaging rules linking micro and macro stresses [51] as well as micro and macro strains [46].

This concept can be readily extended towards multiscale homogenization theory [52], where a material phase observed at scale “A” displays a heterogeneous microstructure at a smaller scale “B”. The mechanical properties of this micro-heterogeneous phase can be identified from an RVE with a characteristic length that is either smaller or equal to the characteristic length of the aforementioned phase.

3.2. Micromechanical representation of mature slag-based CEM II concrete

The three-scale representation depicted in Fig. 3 has been very useful for OPC-based concretes, in particular so for their elastic [26,53,54] and thermo-mechanical [41,55], as well as their short-term creep properties [9,55]. This representation, which is consistent with the scale separation condition of Eq. (2) and the two-scale representation of cement paste introduced in [26], is now adopted for CEM II concretes, with the three RVEs exhibiting the following characteristics:

- Concrete is a matrix-inclusion composite consisting of spherical aggregate inclusions embedded in a cement paste matrix, see Fig. 3(c). Since the aggregates have a maximum size amounting to some 2 cm, the characteristic size of an RVE of concrete amounts to some 6 cm.
- Cement paste is a matrix-inclusion composite consisting of spherical clinker, slag, and limestone inclusions embedded in a hydrate foam matrix, see Fig. 3(b). Since the characteristic sizes of clinker, slag, and limestone particles amount to some tens of microns [40], the characteristic size of an RVE of cement paste amounts to some 0.1 mm.
- The hydrate foam is a highly disordered arrangement of isotropically oriented needle phases representing CEM II hydrates, in direct interaction with spherical capillary pores [26], see Fig. 3(a). Since the characteristic length of the hydrate needles does not exceed a few microns, the characteristic size of an RVE of the hydrate foam amounts to some 20 µm.

The homogenization of linear elasticity according to the RVEs defined in Fig. 3 is performed in a three-step fashion:

Homogenization step I yields the elastic stiffness tensor of hydrate foam according to Fig. 3(a): $\mathbb{C}_{hf}$. By use of a self-consistent scheme [15,56,57], mutual mechanical interactions between all material phases in the RVE are considered, and this is mathematically realized by approximating the material phases as inclusions in auxiliary matrix-inclusion problems of the Eshelby type [58], with the matrix stiffness being set equal to the overall, homogenized elastic stiffness of the hydrate foam itself. Considering spherical capillary pores and an infinite amount of hydrate needles oriented in all space directions indicated by polar angles ϕ and ϑ results in the following implicit expression for the homogenized elastic stiffness tensor of hydrate foam [26,59]:

$$\begin{aligned}\mathbb{C}_{hf} =& \Bigg(f^{hf}_{por}\,\mathbb{C}_{por} : \Big\{\mathbb{I} + \mathbb{P}_{sph} : [\mathbb{C}_{por} - \mathbb{C}_{hf}]\Big\}^{-1} \\ &+ f^{hf}_{hyd}\mathbb{C}_{hyd} : \int_0^{2\pi}\!\!\int_0^{\pi} \Big\{\mathbb{I} + \mathbb{P}_{cyl}(\phi,\vartheta) : [\mathbb{C}_{hyd} - \mathbb{C}_{hf}]\Big\}^{-1} \frac{\sin\vartheta}{4\pi}\,\mathrm{d}\vartheta\mathrm{d}\phi \Bigg) \\ &: \Bigg(f^{hf}_{por}\Big\{\mathbb{I} + \mathbb{P}_{sph} : [\mathbb{C}_{por} - \mathbb{C}_{hf}]\Big\}^{-1} \\ &+ f^{hf}_{hyd} \int_0^{2\pi}\!\!\int_0^{\pi} \Big\{\mathbb{I} + \mathbb{P}_{cyl}(\phi,\vartheta) : [\mathbb{C}_{hyd} - \mathbb{C}_{hf}]\Big\}^{-1} \frac{\sin\vartheta}{4\pi}\,\mathrm{d}\vartheta\mathrm{d}\phi \Bigg)^{-1}, \end{aligned} \tag{3}$$

where f^{hf}_{por} and f^{hf}_{hyd} are the hydrate foam-specific volume fractions of the capillary pores and the hydrates. $\mathbb{P}_{sph}$ and $\mathbb{P}_{cyl}$ are the fourth-order Hill tensors for spherical and cylindrical inclusions, see [9] for mathematical details, $\mathbb{I}$ is the fourth-order identity tensor, exhibiting the components $I_{ijkl} = 1/2\,(\delta_{ik}\delta_{jl} + \delta_{il}\delta_{jk})$, with the Kronecker delta

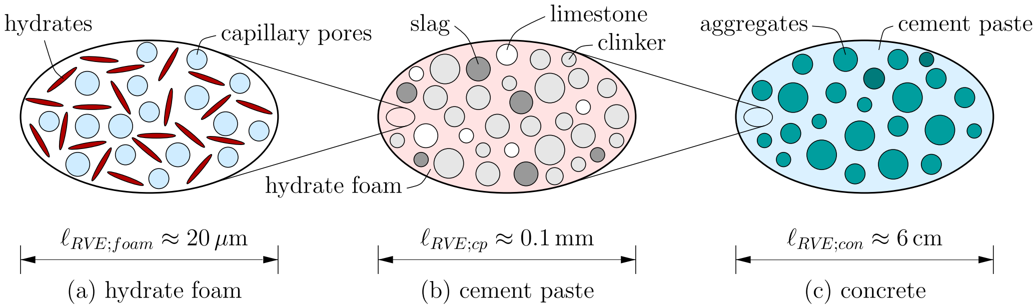

Fig. 3. Micromechanical representation of slag-based CEM II concrete: (a) RVE of hydrate foam built up of spherical capillary pores and needle-shaped CEM II hydrate phases oriented uniformly in all space directions, (b) RVE of cement paste consisting of a hydrate foam matrix with spherical clinker, slag, and limestone inclusions, and (c) RVE of concrete consisting of a cement paste matrix with spherical aggregate inclusions; all schematic 2D sketches refer to 3D volume elements.

being one for $i = j$ and zero otherwise, and ":" is the tensor contraction operator of second order. The material phases are approximately isotropic, so that the elastic stiffness tensors take the form

$$\mathbb{C}_i = 3\,k_i\,\mathbb{I}_{vol} + 2\,\mu_i\,\mathbb{I}_{dev}\,, \tag{4}$$

with $i \in \{hyd, por\}$, with $\mathbb{I}_{vol} = 1/3\,(\mathbf{1} \otimes \mathbf{1})$ and $\mathbb{I}_{dev} = \mathbb{I} - \mathbb{I}_{vol}$ as the volumetric and the deviatoric part of the fourth-order identity tensor $\mathbb{I}$, with $\mathbf{1}$ as the second-order identity tensor, and with k_i and μ_i as the elastic bulk and shear moduli, see Table 1.

Homogenization step II yields the homogenized elastic stiffness tensor of cement paste according to Fig. 3(b): $\mathbb{C}_{cp}$. By use of a Mori–Tanaka scheme [15,60,61], spherical clinker, slag, and limestone inclusions are embedded into the matrix phase, whereby the stiffness of the latter is set equal to the homogenized elastic stiffness of the hydrate foam identified in homogenization step I. This results in the following expression for the elastic stiffness tensor of cement paste:

$$\begin{aligned}\mathbb{C}_{cp} = &\bigg(f^{cp}_{hf}\,\mathbb{C}_{hf} + f^{cp}_{cli}\mathbb{C}_{cli} : \Big\{\mathbb{I} + \mathbb{P}_{sph} : \big[\mathbb{C}_{cli} - \mathbb{C}_{hf}\big]\Big\}^{-1} \\ &+ f^{cp}_{slg}\mathbb{C}_{slg} : \Big\{\mathbb{I} + \mathbb{P}_{sph} : \big[\mathbb{C}_{slg} - \mathbb{C}_{hf}\big]\Big\}^{-1} \\ &+ f^{cp}_{lim}\mathbb{C}_{lim} : \Big\{\mathbb{I} + \mathbb{P}_{sph} : \big[\mathbb{C}_{lim} - \mathbb{C}_{hf}\big]\Big\}^{-1} \bigg) \\ &: \bigg(f^{cp}_{hf}\,\mathbb{I} + f^{cp}_{cli}\Big\{\mathbb{I} + \mathbb{P}_{sph} : \big[\mathbb{C}_{cli} - \mathbb{C}_{hf}\big]\Big\}^{-1} \\ &+ f^{cp}_{slg}\Big\{\mathbb{I} + \mathbb{P}_{sph} : \big[\mathbb{C}_{slg} - \mathbb{C}_{hf}\big]\Big\}^{-1} \\ &+ f^{cp}_{lim}\Big\{\mathbb{I} + \mathbb{P}_{sph} : \big[\mathbb{C}_{lim} - \mathbb{C}_{hf}\big]\Big\}^{-1} \bigg)^{-1}, \end{aligned} \tag{5}$$

where f^{cp}_i with $i \in \{cli, slg, lim, hf\}$ are the cement paste-specific volume fractions of clinker, slag, limestone, and of the hydrate foam matrix. The stiffness of the latter results from the previous homogenization step according to Eq. (3), while the stiffness tensors of clinker, slag, and limestone follow from specification of Eq. (4) for $\in \{cli, slg, lim\}$, together with the corresponding values reported in Table 1.

Homogenization step III yields the elastic stiffness tensor of concrete according to Fig. 3(c): $\mathbb{C}_{con}$. By use of a Mori–Tanaka scheme [15,60], six types of aggregate inclusions (described in more detail in Section 3.3) are embedded into a contiguous matrix phase, whereby the stiffness of the latter is set equal to that of the homogenized elastic stiffness of cement paste identified in step II. This results in the following expression for the homogenized elastic stiffness tensor of concrete:

$$\begin{aligned}\mathbb{C}_{con} = &\bigg(f^{con}_{cp}\,\mathbb{C}_{cp} + \sum_j f^{con}_j \mathbb{C}_j : \Big\{\mathbb{I} + \mathbb{P}_{sph} : \big[\mathbb{C}_j - \mathbb{C}_{cp}\big]\Big\}^{-1} \bigg) \\ &: \bigg(f^{con}_{cp}\,\mathbb{I} + \sum_j f^{con}_j \Big\{\mathbb{I} + \mathbb{P}_{sph} : \big[\mathbb{C}_j - \mathbb{C}_{cp}\big]\Big\}^{-1} \bigg)^{-1}, \end{aligned} \tag{6}$$

where f^{con}_{cp} and f^{con}_j with $j \in \{lim, dol, grt, qzt, blt, dbs\}$ are the concrete-specific volume fractions of the cement paste matrix and of the aggregates, where the stiffness tensor of the cement paste, $\mathbb{C}_{cp}$, results from the previous homogenization step according to Eq. (5), and where the stiffness tensors of the aggregate types, $\mathbb{C}_j$, follow from specification of Eq. (4) for $j \in \{lim, dol, grt, qzt, blt, dbs\}$, together with corresponding values reported in Table 1. This isotropic elastic stiffness tensor can be fully described by two independent stiffness values, such as the tensor components C_{1111} and C_{1212}. They can be transformed into the elastic bulk and shear moduli, k_{con} and μ_{con}, via

$$k_{con} = C_{1111} - \frac{2}{3}C_{1212}\,, \qquad \mu_{con} = \frac{C_{1212}}{2}\,, \tag{7}$$

and into the elastic Young's modulus E_{con} and Poisson's ratio ν_{con} via

$$E_{con} = \frac{1}{D_{1111}}\,, \qquad \nu_{con} = \frac{D_{1122}}{D_{1111}}\,, \tag{8}$$

where D_{1111} and D_{1122} are components of the elastic compliance tensor, which is defined as the inverse of the elastic stiffness tensor: $\mathbb{D}_{con} = \mathbb{C}^{-1}_{con}$.

3.3. Adapted Powers-Acker hydration model: RVE-specific volume fractions

The hydration products of slag-based CEM II cements result from the reaction of two constituents, namely Portland clinker and slag, with water. A corresponding, calorimetry-based hydration model for slag-blended cements [40] has evidenced the sum of the clinker and slag volumes to decrease linearly with the hydration degree. This, together with the remarkable similarity between the isothermal hydration heat evolutions of CEM I and CEM II [62], motivates us to consider both constituents as one chemical unit, referred to as "reac" in the following, and to describe its hydration by means of a modified version of the Powers-Acker hydration model [31,53,57,63]. This modification provides relations between the hydration degree and the corresponding volume fractions of unhydrated reactants, of limestone, of water, of air, and of hydration products. The aforementioned relations follow from the subsequent considerations:

The initial volume fraction of reactants in a volume of cement paste at zero hydration degree, $\xi = 0$, reads as

$$\begin{aligned} f^{cp}_{reac}(\xi = 0) &= \frac{V_{cli}(\xi = 0) + V_{slg}(\xi = 0)}{V_{cp}} \\ &= \frac{1 + \dfrac{\rho_{cli}}{\rho_{slg}}\dfrac{m_{slg}}{m_{cli}}}{1 + \dfrac{\rho_{cli}}{\rho_{slg}}\dfrac{m_{slg}}{m_{cli}} + \dfrac{\rho_{cli}}{\rho_{H_2O}}\dfrac{m_{H_2O}}{m_{cli}} + \dfrac{\rho_{cli}}{\rho_{lim}}\dfrac{m_{lim}}{m_{cli}}}\,, \end{aligned} \tag{9}$$

with V_{cp} as the volume of cement paste, which stays constant over the hydration process and which is equal to the sum of the initial volumes of reactants, of limestone, and of water,

$$V_{cp} = V_{cli}(\xi = 0) + V_{slg}(\xi = 0) + V_{H_2O}(\xi = 0) + V_{lim}\,. \tag{10}$$

Furthermore, m_{H_2O}/m_{cli} in Eq. (9) denotes the initial water-to-clinker mass ratio, m_{slg}/m_{cli} denotes the initial slag-to-clinker mass ratio, and m_{lim}/m_{cli} denotes the initial limestone-to-clinker mass ratio, see Tables 2 and 4 for the concretes dealt with in the present contribution;

Table 5
Mixture-independent mass densities of constituents of CEM II cement paste.

Constituent		ρ_i [g/cm^3]	Ref.
clinker	$i = cli$	3.150	[26,32]
slag	$i = slg$	2.800	[40]
limestone	$i = lim$	2.701	[64]
water	$i = \mathrm{H_2O}$	1.000	[26,32,40]
hydrates	$i = hyd$	2.073	[26,32]

$\rho_{\mathrm{H_2O}}$ denotes the mass density of water, while ρ_{cli}, ρ_{slg}, and ρ_{lim} denote the mass densities of clinker, of slag, and of limestone, respectively, see Table 5. The mass density of the reactants, ρ_{reac}, can be determined from the average rule for mass densities, reading for the slag-clinker system as

$$\rho_{reac} = f_{cli}^{reac}\,\rho_{cli} + f_{slg}^{reac}\,\rho_{slg}\,, \tag{11}$$

where the volume fractions of clinker and of slag inside a volume of slag-clinker reactants, f_{cli}^{reac} and f_{slg}^{reac}, fulfill

$$f_{cli}^{reac} = \frac{1}{1+\frac{\rho_{cli}}{\rho_{slg}}\left(\frac{m_{slg}}{m_{cli}}\right)(\xi=0)}\,, \tag{12}$$

and

$$f_{slg}^{reac} = 1 - f_{cli}^{reac}\,. \tag{13}$$

The mass density of the reactants can then be expressed as

$$\rho_{reac} = \frac{1+\left(\frac{m_{slg}}{m_{cli}}\right)(\xi=0)}{1+\frac{\rho_{cli}}{\rho_{slg}}\left(\frac{m_{slg}}{m_{cli}}\right)(\xi=0)}\,\rho_{cli}\,. \tag{14}$$

When defining the hydration degree ξ as the mass of already hydrated reactants over their initial mass [9,53], the hydration-dependent volume fraction of unhydrated reactants in a volume of cement paste reads as

$$f_{reac}^{cp} = \frac{\left(1+\frac{\rho_{cli}}{\rho_{slg}}\frac{m_{slg}}{m_{cli}}\right)(1-\xi)}{1+\frac{\rho_{cli}}{\rho_{slg}}\frac{m_{slg}}{m_{cli}}+\frac{\rho_{cli}}{\rho_{\mathrm{H_2O}}}\frac{m_{\mathrm{H_2O}}}{m_{cli}}+\frac{\rho_{cli}}{\rho_{lim}}\frac{m_{lim}}{m_{cli}}}\,. \tag{15}$$

The volume fraction of limestone in a volume of cement paste is correspondingly found as

$$f_{lim}^{cp} = \frac{\frac{\rho_{cli}}{\rho_{lim}}\frac{m_{lim}}{m_{cli}}}{1+\frac{\rho_{cli}}{\rho_{slg}}\frac{m_{slg}}{m_{cli}}+\frac{\rho_{cli}}{\rho_{\mathrm{H_2O}}}\frac{m_{\mathrm{H_2O}}}{m_{cli}}+\frac{\rho_{cli}}{\rho_{lim}}\frac{m_{lim}}{m_{cli}}}\,. \tag{16}$$

During the hydration of standard OPC systems, one mass unit of water combines with 0.42 mass units of clinker [53]. The similarities between CEM I and CEM II hydration [40,62] motivate us to adopt the same mass ratio value for CEM II, which implies the following mathematical relation:

$$\frac{dm_{\mathrm{H_2O}}}{d\xi} = 0.42\frac{dm_{reac}}{d\xi}\,. \tag{17}$$

The mass of reactants can be expressed by the volume fraction of reactants within a volume of cement paste,

$$m_{reac} = \rho_{reac}\,f_{reac}^{cp}\,V_{cp} = \frac{\rho_{reac}\,V_{cp}\left(1+\frac{\rho_{cli}}{\rho_{slg}}\frac{m_{slg}}{m_{cli}}\right)(1-\xi)}{1+\frac{\rho_{cli}}{\rho_{slg}}\frac{m_{slg}}{m_{cli}}+\frac{\rho_{cli}}{\rho_{\mathrm{H_2O}}}\frac{m_{\mathrm{H_2O}}}{m_{cli}}+\frac{\rho_{cli}}{\rho_{lim}}\frac{m_{lim}}{m_{cli}}}\,, \tag{18}$$

where we made also use of Eq. (15). Insertion of Eq. (18) into Eq. (17) and subsequent temporal integration yields the hydration-dependent mass of water as

$$m_{\mathrm{H_2O}} = m_{\mathrm{H_2O}}(\xi=0) - \frac{0.42\,\rho_{reac}\,V_{cp}\left(1+\frac{\rho_{cli}}{\rho_{slg}}\frac{m_{slg}}{m_{cli}}\right)\xi}{1+\frac{\rho_{cli}}{\rho_{slg}}\frac{m_{slg}}{m_{cli}}+\frac{\rho_{cli}}{\rho_{\mathrm{H_2O}}}\frac{m_{\mathrm{H_2O}}}{m_{cli}}+\frac{\rho_{cli}}{\rho_{lim}}\frac{m_{lim}}{m_{cli}}}\,. \tag{19}$$

Setting this relation equal to the mass of water expressed through its volume fraction, namely to

$$m_{\mathrm{H_2O}} = \rho_{\mathrm{H_2O}}\,f_{\mathrm{H_2O}}^{cp}\,V_{cp}\,, \tag{20}$$

gives access to the hydration degree-dependent volume fraction of water, as function of its initial value, of the constituent mass densities, and of the initial water-to-clinker, slag-to-clinker, and limestone-to-clinker mass ratios; mathematically, this reads as

$$f_{\mathrm{H_2O}}^{cp} = f_{\mathrm{H_2O}}^{cp}(\xi=0) - \frac{0.42\,\frac{\rho_{reac}}{\rho_{\mathrm{H_2O}}}\left(1+\frac{\rho_{cli}}{\rho_{slg}}\frac{m_{slg}}{m_{cli}}\right)\xi}{1+\frac{\rho_{cli}}{\rho_{slg}}\frac{m_{slg}}{m_{cli}}+\frac{\rho_{cli}}{\rho_{\mathrm{H_2O}}}\frac{m_{\mathrm{H_2O}}}{m_{cli}}+\frac{\rho_{cli}}{\rho_{lim}}\frac{m_{lim}}{m_{cli}}}\,. \tag{21}$$

Dividing Eq. (10) by V_{cp} and rearranging the resulting expression for the volume fraction of water yields

$$f_{\mathrm{H_2O}}^{cp}(\xi=0) = 1 - f_{reac}^{cp}(\xi=0) - f_{lim}^{cp}\,, \tag{22}$$

and use of this relation in Eq. (21), together with Eq. (9), yields

$$f_{\mathrm{H_2O}}^{cp} = \frac{\frac{\rho_{cli}}{\rho_{\mathrm{H_2O}}}\frac{m_{\mathrm{H_2O}}}{m_{cli}} - 0.42\frac{\rho_{reac}}{\rho_{\mathrm{H_2O}}}\left(1+\frac{\rho_{cli}}{\rho_{slg}}\frac{m_{slg}}{m_{cli}}\right)\xi}{1+\frac{\rho_{cli}}{\rho_{slg}}\frac{m_{slg}}{m_{cli}}+\frac{\rho_{cli}}{\rho_{\mathrm{H_2O}}}\frac{m_{\mathrm{H_2O}}}{m_{cli}}+\frac{\rho_{cli}}{\rho_{lim}}\frac{m_{lim}}{m_{cli}}}\,. \tag{23}$$

During hydration, as quantified through increasing values of ξ, the total mass within an RVE of cement paste is conserved. Initially, this mass is composed of the masses of cement and of water only, and as soon as the hydration reaction starts, hydrates with mass m_{hyd} are formed; mathematically, this reads as

$$m_{reac}(\xi=0)+m_{\mathrm{H_2O}}(\xi=0)+m_{lim} = m_{reac}(\xi)+m_{\mathrm{H_2O}}(\xi)+m_{lim}+m_{hyd}(\xi)\,. \tag{24}$$

The masses of limestone, of water, of reactants, and of hydration products can be expressed in terms of the respective volume fractions, via

$$m_i = f_i\rho_iV_{cp}\,,\qquad i\in\{reac, hyd, \mathrm{H_2O}\}\,, \tag{25}$$

and use of Eq. (25) in Eq. (24) provides an expression for the volume fraction of the hydrates, reading as

$$f_{hyd}^{cp} = \frac{\rho_{reac}}{\rho_{hyd}}\left[f_{reac}^{cp}(\xi=0) - f_{reac}^{cp}(\xi)\right] + \frac{\rho_{\mathrm{H_2O}}}{\rho_{hyd}}\left[f_{\mathrm{H_2O}}^{cp}(\xi=0) - f_{\mathrm{H_2O}}^{cp}(\xi)\right]. \tag{26}$$

Insertion of Eqs. (15) and (23) into Eq. (26) eventually yields

$$f_{hyd}^{cp} = \frac{1.42\,\frac{\rho_{reac}}{\rho_{hyd}}\left(1+\frac{\rho_{cli}}{\rho_{slg}}\frac{m_{slg}}{m_{cli}}\right)\xi}{1+\frac{\rho_{cli}}{\rho_{slg}}\frac{m_{slg}}{m_{cli}}+\frac{\rho_{cli}}{\rho_{\mathrm{H_2O}}}\frac{m_{\mathrm{H_2O}}}{m_{cli}}+\frac{\rho_{cli}}{\rho_{lim}}\frac{m_{lim}}{m_{cli}}}\,, \tag{27}$$

with ρ_{hyd} as the mass density of the hydrates, see Table 5. The sum of the volumes of cement and water forming a new volume of hydrates is larger than the volume of the newly formed hydrates. This is referred to as the Le Chatelier contraction [65–67]. Hence, while the volume of cement paste remains virtually constant throughout the hydration reaction, and while the hydrates do not occupy the entire space which was filled by their reactants, a new phase, hosting air and quantified by volume fraction f_{air}^{cp}, is established. Mathematically, this reads as

$$f_{reac}^{cp} + f_{lim}^{cp} + f_{\mathrm{H_2O}}^{cp} + f_{hyd}^{cp} + f_{air}^{cp} = 1\,. \tag{28}$$

Insertion of Eqs. (15), (23), and (27) into Eq. (28), and rearranging for the volume fraction of the air pores yields

$$f_{air}^{cp} = \frac{\left(1+0.42\frac{\rho_{reac}}{\rho_{\mathrm{H_2O}}} - 1.42\frac{\rho_{reac}}{\rho_{hyd}}\right)\left(1+\frac{\rho_{cli}}{\rho_{slg}}\frac{m_{slg}}{m_{cli}}\right)\xi}{1+\frac{\rho_{cli}}{\rho_{slg}}\frac{m_{slg}}{m_{cli}}+\frac{\rho_{cli}}{\rho_{\mathrm{H_2O}}}\frac{m_{\mathrm{H_2O}}}{m_{cli}}+\frac{\rho_{cli}}{\rho_{lim}}\frac{m_{lim}}{m_{cli}}}\,. \tag{29}$$

Furthermore, our current mechanical analysis is restricted to drained conditions where neither the water-filled pores nor the air pores carry any loads. Hence, these two pore types behave, mechanically speaking,

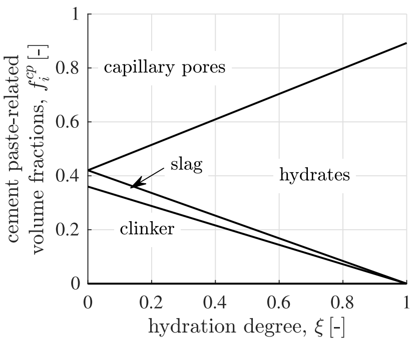

Fig. 4. Cement paste-related volume fractions of the CEM II-based concrete used with construction lot KAT3 [29], f_i^{cp}, as functions of the hydration degree, ξ; and for initial mass ratios of $m_{H_2O}/m_{cli} = 0.51$, $m_{slg}/m_{cli} = 0.15$, and $m_{lim}/m_{cli} = 0$, see also Table 2.

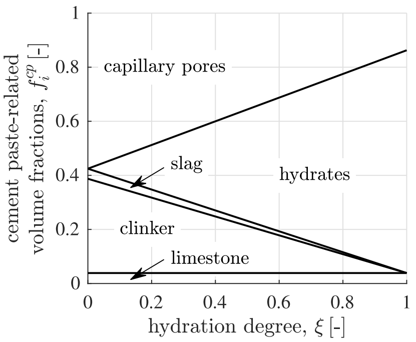

Fig. 5. Cement paste-related volume fractions of the CEM II-based concrete investigated by Dummer et al. [30], f_i^{cp}, as functions of the hydration degree, ξ; and for initial mass ratios of $m_{H_2O}/m_{cli} = 0.52$, $m_{slg}/m_{cli} = 0.1$, and $m_{lim}/m_{cli} = 0.1$, see also Table 4.

in the very same manner, which motivates us to combine them into one single phase, denoted by "*por*", with the volume fraction,

$$f_{por}^{cp} = \frac{\dfrac{\rho_{cli}}{\rho_{H_2O}}\dfrac{m_{H_2O}}{m_{cli}} + \left(1 - 1.42\dfrac{\rho_{reac}}{\rho_{hyd}}\right)\left(1 + \dfrac{\rho_{cli}}{\rho_{slg}}\dfrac{m_{slg}}{m_{cli}}\right)\xi}{1 + \dfrac{\rho_{cli}}{\rho_{slg}}\dfrac{m_{slg}}{m_{cli}} + \dfrac{\rho_{cli}}{\rho_{H_2O}}\dfrac{m_{H_2O}}{m_{cli}} + \dfrac{\rho_{cli}}{\rho_{lim}}\dfrac{m_{lim}}{m_{cli}}}\,. \tag{30}$$

The two portions of unhydrated CEM II, namely Portland clinker and slag, show significantly different elastic moduli, see Table 1, so that we need to determine the volume fractions of clinker and slag, as appearing in Eq. (5). Therefore, we resort to the cement paste-specific volume fractions according to Eqs. (12) and (13), from which we arrive at

$$f_{cli}^{cp} = f_{cli}^{reac} f_{reac}^{cp}\,, \qquad f_{slg}^{cp} = f_{slg}^{reac} f_{reac}^{cp}\,. \tag{31}$$

It is useful to illustrate the functional dependence of the paste-related volume fractions on the hydration degree, see Fig. 4 for the concrete used with construction lot KAT3 [29], according to Table 2, and Fig. 5 for the concrete from Dummer et al. [30], according to Table 4. We add that the cement paste-specific volume fraction of hydrate foam, f_{hf}^{cp}, occurring in Eq. (5) is computed according to

$$f_{hf}^{cp} = f_{por}^{cp} + f_{hyd}^{cp}\,. \tag{32}$$

The concrete-related volume fraction of cement paste, denoted as f_{cp}^{con}, is independent of the hydration degree, and can be expressed by the initial apparent mass density of cement paste in concrete, denoted as $\rho_{cp}^{con}(\xi = 0)$, i.e., the mass of CEM II and water at zero hydration per volume of concrete, which is known from the concrete mix design, and by the initial mass density of cement paste, denoted as $\rho_{cp}(\xi = 0)$. In mathematical terms, this reads as

$$f_{cp}^{con} = \frac{\rho_{cp}^{con}(\xi = 0)}{\rho_{cp}(\xi = 0)}\,, \tag{33}$$

whereby the initial apparent mass density of cement paste in concrete follows from

$$\rho_{cp}^{con}(\xi = 0) = \rho_{cemII}^{con}(\xi = 0) + \rho_{H_2O}^{con}(\xi = 0)\,, \tag{34}$$

with $\rho_{cemII}^{con}(\xi = 0)$ and $\rho_{H_2O}^{con}(\xi = 0)$ as the initial apparent mass densities of CEM II and water, see Tables 2 and 4 for the concretes investigated herein; and the initial mass density of cement paste follows from the average rule for mass densities

$$\rho_{cp}(\xi = 0) = \rho_{reac}\, f_{reac}^{cp}(\xi = 0) + \rho_{H_2O}\, f_{H_2O}^{cp}(\xi = 0) + \rho_{lim}\, f_{lim}^{cp}\,, \tag{35}$$

with $f_{reac}^{cp}(\xi = 0)$ according to Eq. (9). The volume fraction of aggregates is then readily provided by

$$f_{agg}^{con} = 1 - f_{cp}^{con}\,, \tag{36}$$

Since several aggregate types with different elastic properties are used, the aggregate volume fraction needs to be subdivided, with f_j^{agg}, $j \in \{lim, dol, grt, qzt, blt, dbs\}$ as the volume fractions of the different aggregate types. The latter are approximated by the mass fractions known from weighing tests, since the mass densities of the individual aggregate types are very similar, see Tables 2 and 4 for the concretes investigated herein. At the concrete level, the corresponding volume fractions read as

$$f_j^{con} = f_j^{agg}(1 - f_{cp}^{con})\,, \tag{37}$$

see Table 6 for the concrete-related volume fractions of the concretes investigated herein.

Table 6
Concrete-related volume fractions for the concretes investigated herein.

KAT3 construction lot [29]	
dolomite	$f_{dol}^{con} = 0.198$
limestone	$f_{lim}^{con} = 0.198$
granite	$f_{grt}^{con} = 0.095$
quarzite	$f_{qzt}^{con} = 0.080$
basalt	$f_{blt}^{con} = 0.075$
diabase	$f_{dbs}^{con} = 0.070$
cement paste	$f_{cp}^{con} = 0.284$
Concrete investigated by Dummer et al. [30]	
limestone	$f_{lim}^{con} = 0.713$
cement paste	$f_{cp}^{con} = 0.287$

Finally, the hydrate foam-related volume fractions of the capillary pores, f_{por}^{hf}, and the hydrates, f_{hyd}^{hf}, read as [26]

$$f_{por}^{hf} = \frac{f_{por}^{cp}}{1 - f_{reac}^{cp} - f_{lim}^{cp}}\,, \qquad f_{hyd}^{hf} = \frac{f_{hyd}^{cp}}{1 - f_{reac}^{cp} - f_{lim}^{cp}}\,. \tag{38}$$

3.4. Multiscale model-enabled identification of the hydration degree

The composition of the microstructure of concrete changes with ongoing hydration of cement paste, see Figs. 4 and 5. The state of this process is described by the hydration degree ξ. The latter evolves with the age of the considered concrete. The corresponding chemical kinetics can be quantified by Arrhenius-type evolution equations [68], together with calorimetry testing protocols [40,69,70]. In general, the hydration degree of concrete which is older than a few days is not directly accessible from experiments. As a remedy, the microelastic model of Section 3.2, together with experimentally determined values of the elastic moduli of the investigated CEM II concrete, the isothermal modulus evolution rule from the fib Model Code [71], and the hydration model of Section 3.3, will be used in the following, so as to re-construct the evolution of the hydration degree during the herein studied long-term creep tests on CEM II concretes.

In more detail, Eq. (8) together with Eqs. (6), (5), and (3), gives the macroscopic elastic Young's modulus of concrete as a function of the phase volume fractions, which, via Eqs. (15), (16), (27), and (30),

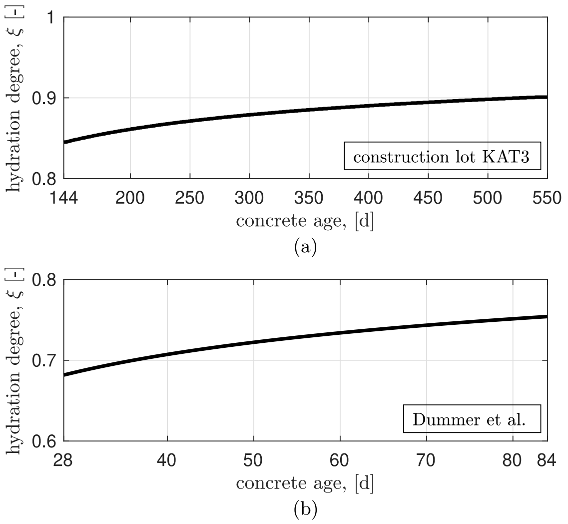

Fig. 6. Evolution of hydration degree in CEM II concretes tested (a) at KAT3 construction lot [29] and (b) by Dummer et al. [30].

depend on the hydration degree. This yields the macroscopic elastic Young's modulus as a function of the hydration degree, $E_{con}(\xi)$.

In order to transform the relation $E_{con}(\xi)$ into an evolution of the hydration degree, $\xi(t)$, the evolution of the elastic modulus is needed. For isothermal conditions at 20°C, which do approximately prevail in the presently investigated cases, the evolution of the elastic modulus over time can be mathematically described by the fib Model Code [71] according to

$$E_{con}(t) = E_{con,28\text{d}} \left\{ \exp\left(s \left[1 - \sqrt{\frac{28\,\text{d}}{t}} \right] \right) \right\}^{0.5}, \tag{39}$$

where $E_{con,28\text{d}}$ denotes the elastic Young's modulus at a concrete age of 28 days and s denotes a dimensionless parameter related to the speed with which the 28-day stiffness is approached. It amounts to $s = 0.25$ for cement type 42.5N and to $s = 0.2$ for cement type 52.5N. As for the concrete investigated by Dummer et al. [30], the experimentally determined value of $E_{con,28\text{d}} = 30.3\,\text{GPa}$ is directly reported, while Razgordanisharahi et al. [29] reported an elastic modulus reached after 144 days, $E_{con,144\text{d}} = 37.8\,\text{GPa}$ for the CEM II concrete used at KAT 3 construction lot. Insertion of this value into Eq. (39) yields a corresponding 28-day value of $E_{con,28\text{d}} = 35.7\,\text{GPa}$. Based on these 28-day moduli, both $E_{con}(t)$, via Eq. (39), and $E_{con}(\xi)$, via the microelastic model of Section 3.2 together with the hydration model of Section 3.3 are known. Setting corresponding functional values equal to each other yields hydration degree values for different points in time; mathematically, this reads as

$$E_{con}(t) = E_{con}(\xi) \quad \rightarrow \quad \xi(t)\,, \tag{40}$$

see Fig. 6 for an illustration of the respective evolutions of the hydration degree during the creep tests analyzed herein.

4. Identification of creep properties of CEM II hydrates, via multiscale aging viscoelastic modeling

4.1. Temperature-activated short-to-long-term creep of hydrates

Basic creep properties of concrete made from CEM I are governed by the viscoelastic behavior of the hydrates [9–12], i.e., the products of the chemical reaction between clinker and water. For the determination of the hydrate creep properties, an experimental campaign consisting of three-minute-long creep tests on CEM I cement pastes with different initial water-to-cement mass ratios and different maturity degrees turned out as very useful [72]. Over this short observation time, the microstructure of the tested cement paste did not significantly change, regardless of the actual progress of the hydration reactions [73]. The corresponding short-term creep behavior of the tested cement pastes was almost perfectly represented by a uniaxial power-law creep function [9,74]. This macroscopically determined non-aging creep function was then implemented into a micro-viscoelastic model with phases as seen in Fig. 3, while assigning viscoelastic properties to the hydrate phases, the hydrate foam phase, and the cement paste phase. This allowed for identification of a universal isochoric non-aging creep tensor function of CEM I hydrates [9], reading as

$$\mathbb{J}_{hyd}(t-\tau) = \frac{1}{3\,k_{hyd}}\mathbb{I}_{vol} + \frac{1}{2}\left[\frac{1}{\mu_{hyd}} + \frac{1}{\mu_{c,hyd}}\left(\frac{t-\tau}{t_{ref}}\right)^{\beta}\right]\mathbb{I}_{dev}\,, \tag{41}$$

where k_{hyd} and μ_{hyd} stand for the elastic bulk and shear modulus of hydrates [26], and $\mu_{c,hyd} = 20.93\,\text{GPa}$ stands for the shear creep modulus of CEM I hydrates [9]. The reference time is set equal to $t_{ref} = 1\,\text{d}$ with "d" standing for the physical unit "day". The power-law creep exponent of hydrates β has been shown to be virtually invariant for widely varying cementitious mixtures, as well as across length scales, all the way down to the hydrate scale [9]: $\beta = 0.25$. This reflects the typical load-carrying behavior of concrete, where virtually no (micro-)load transfer takes place from the creeping hydrate phases to any of the non-creeping material constituents, such as the cement grains or the aggregates [55].

The non-aging creep tensor function of CEM I hydrates (41) is herein extended towards (i) consideration of short-to-long-term creep by means of a piecewisely defined function comprising a power law for the short-term portion and a logarithmic law for the long-term portion [8,29,72,75,76], towards (ii) consideration of the temperature dependence of hydrate properties in the line of [55], and towards (iii) consideration of the influence of (time-invariant, but test-specific) relative humidity $\varphi \in \{0;1\}$ on the shear creep modulus of hydrates. This extended version of Eq. (41) is applied to hydrates made from CEM II/A-S 52.5 N, with the corresponding shear creep modulus being denoted as $\mu^{II}_{c,hyd}(\varphi, T)$. The extended universal isochoric non-aging creep tensor function of CEM II hydrates reads as

$$\mathbb{J}^{II}_{hyd}(t-\tau) = \frac{1}{3\,k_{hyd}(T)}\mathbb{I}_{vol} + \frac{1}{2}\left[\frac{1}{\mu_{hyd}(T)} + \frac{F(t-\tau)}{\mu^{II}_{c,hyd}(\varphi,T)}\right]\mathbb{I}_{dev}\,, \tag{42}$$

with the piecewisely defined function $F(t-\tau)$ reading as

$$F(t-\tau) = \begin{cases} \left(\dfrac{t-\tau}{t_{ref}}\right)^{\beta} & \dots \quad \tau \le t \le \tau + t_{tst}\,, \\[2ex] C\,\ln\left(1 + B\,\dfrac{t-\tau}{t_{tst}}\right) & \dots \quad t \ge \tau + t_{tst}\,, \end{cases} \tag{43}$$

where t_{tst} denotes the transition time instant, marking the shift from power law type to logarithmic creep behavior. As for cement pastes, t_{tst} was identified to lie between 20 and 45 days [72]. Given the absence of (micro-)load transfer from the creeping hydrate phases to any of the non-creeping material constituents [55], the transition time instant is expected to be virtually invariant across length scales, so that we here adopt a mean value of $t_{tst} = 32\,\text{d}$ for the concrete tested in Koralm tunnel KAT3, see also [29] and Table 7. B and C are dimensionless constants ensuring that $F(t-\tau)$ is a differentiable function at the transition time instant. They depend only on the power law exponent and the transition time. Accordingly, they are also invariant across the length scales of the present multiscale mechanics model for concrete. In mathematical terms, the continuity conditions at time t_{tst} read as

$$\lim_{\epsilon\to 0} F(t_{tst}-\epsilon) = \lim_{\epsilon\to 0} F(t_{tst}+\epsilon)\,, \tag{44}$$

$$\lim_{\epsilon\to 0} \dot{F}(t_{tst}-\epsilon) = \lim_{\epsilon\to 0} \dot{F}(t_{tst}+\epsilon)\,, \tag{45}$$

where a dot denotes derivation with respect to time. Insertion of Eq. (43) into the conditions (44) and (45) yields the following relations

Table 7
Parameters defining the piecewisely defined function $F(t-\tau)$, see Eq. (43).

Model parameter	Symbols	Values
Reference time	t_{ref}	1 d
Power law exponent	β	0.25
Transition time	t_{tst}	32 d
Dimensionless parameter	B	49.44
Dimensionless parameter	C	0.6066

$$\beta = \frac{B}{1+B}\,\frac{1}{\ln(1+B)}\,, \tag{46}$$

$$C = \frac{1}{\ln(1+B)}\left(\frac{t_{tst}}{t_{ref}}\right)^{\beta}. \tag{47}$$

Insertion of the described values of β, t_{ref}, and t_{tst} into Eqs. (46) and (47) yields the dimensionless constants ensuring the smoothness of the piecewisely defined function $F(t-\tau)$ as: $B = 49.44$ and $C = 0.6066$, see also Table 7.

Elastic properties of CEM I cement pastes were shown to depend linearly on temperatures ranging from 283.15 K to 323.15 K (i.e., 10°C to 50°C) [55]. This dependence can be quantified through

$$\frac{E_{hyd}(T)}{E_{hyd}(293\,\mathrm{K})} = 1 + 0.46\left(1 - \frac{T}{293.15\,\mathrm{K}}\right). \tag{48}$$

where T refers to the temperature given in Kelvin. Considering the aforementioned similarities between CEM I and CEM II, we adopt the same linear temperature dependence for the elastic properties of CEM II, yielding

$$k_{hyd}(T) = 18.69\,\mathrm{GPa}\left(1 + 0.46\left(1 - \frac{T}{293.15\,\mathrm{K}}\right)\right), \tag{49}$$

$$\mu_{hyd}(T) = 11.76\,\mathrm{GPa}\left(1 + 0.46\left(1 - \frac{T}{293.15\,\mathrm{K}}\right)\right),$$

The temperature activation of creep properties of the hydrates can be considered through an Arrhenius law with an activation energy being that of bulk water, i.e., $Q = 17.57\,\mathrm{kJ/mol}$ [55]; and creep strains scale linearly with the relative humidity φ [77]. Mathematically, these relations imply the following format of the shear creep modulus of CEM II hydrates:

$$\mu^{II}_{c,hyd}(\varphi, T) = \frac{\tilde{\mu}^{II}_{c,hyd}}{\varphi}\,\exp\left(\frac{Q}{R}\left[\frac{1}{T} - \frac{1}{293.15\,\mathrm{K}}\right]\right), \tag{50}$$

where $R = 8.314\,\mathrm{J/(mol\,K)}$ stands for the universal gas constant, and $\tilde{\mu}^{II}_{c,hyd}$ stands for the shear creep modulus prevailing at 20°C and 100% relative humidity.

4.2. *Homogenization of non-aging viscoelastic material behavior, from the scale of hydrates up to that of concrete*

The hydrate phases depicted in Fig. 3(a), as well as the RVEs in Fig. 3(b) and (c), are considered to exhibit non-aging, linear viscoelastic behavior. The latter is governed by Boltzmanns's integro-differential equation for "delayed elasticity", which reads as [78–80]

$$\boldsymbol{\sigma}(t) = \int_{-\infty}^{t} \mathbb{R}(t-\tau) : \dot{\boldsymbol{\varepsilon}}(\tau)\,\mathrm{d}\tau\,, \quad \boldsymbol{\varepsilon}(t) = \int_{-\infty}^{t} \mathbb{J}(t-\tau) : \dot{\boldsymbol{\sigma}}(\tau)\,\mathrm{d}\tau\,, \tag{51}$$

where $\boldsymbol{\sigma}$ and $\boldsymbol{\varepsilon}$ denote the stress tensor and the linearized strain tensor, associated with the hydrate phases depicted in Fig. 3(a) or with the RVEs in Fig. 3(b) and (c); t denotes the recording time during the creep and relaxation processes, while τ denotes the time instant of loading events that cause delayed effects. The creep compliance tensor $\mathbb{J}$ and the relaxation tensor $\mathbb{R}$ of each constituent fulfill the convolution condition according to Schwarzl–Struik [81]:

$$\int_{-\infty}^{t} \mathbb{J}(t-\tau) : \mathbb{R}(\tau)\,\mathrm{d}\tau = \int_{-\infty}^{t} \mathbb{R}(t-\tau) : \mathbb{J}(\tau)\,\mathrm{d}\tau = t\,\mathbb{I}\,. \tag{52}$$

For the purely elastically behaving phases, i.e., the capillary pores in Fig. 3(a), the clinker, slag, and limestone phases in Fig. 3(b), and the aggregate phases in Fig. 3(c), the convolution integrals in Eq. (51) are reduced to the standard "generalized Hooke's law for elasticity": $\mathbb{R}_i(t-\tau) = \mathbb{R}_i(0) = \mathbb{C}_i$ with $i \in \{por, cli, slg, lim, dol, grt, qzt, blt, dbs\}$ according to Eq. (4).

Upscaling of viscoelastic material behavior from the scale of the hydrates up to that of concrete becomes particularly simple in the Laplace–Carson domain. The Laplace–Carson transform $f^*(p)$ of any time-dependent function $f(t)$ is defined as [82]

$$f^*(p) = p\int_{0}^{\infty} f(t)\exp(-pt)\,\mathrm{d}t\,, \tag{53}$$

with p standing for the complex Laplace–Carson variable. Application of the transformation rule (53) to Boltzmann's superposition principle (51) describing viscoelastic behavior (including the special case of elastic behavior), yields algebraic quasi-elastic constitutive equations for all constituents in the Laplace–Carson domain, reading as

$$\boldsymbol{\sigma}^*(p) = \mathbb{R}^*(p) : \boldsymbol{\varepsilon}^*(p)\,, \quad \boldsymbol{\varepsilon}^*(p) = \mathbb{J}^*(p) : \boldsymbol{\sigma}^*(p)\,. \tag{54}$$

The convolution integral of the Schwarzl–Struik conditions (52) is reduced to a simple algebraic relation between the Laplace–Carson transformed relaxation and creep tensor, which follows from Eq. (54), as [13]

$$\mathbb{R}^*(p) : \mathbb{J}^*(p) = \mathbb{I}\,. \tag{55}$$

The Laplace–Carson transformed creep tensor function of the hydrates results from inserting the creep tensor function of Eq. (42) into the transformation rule of Eq. (53), as

$$\begin{aligned}\mathbb{J}^{*,II}_{hyd}(p,\varphi,T) = {} & \frac{1}{3\,k_{hyd}(T)}\mathbb{I}_{vol} + \frac{1}{2}\Bigg\{\frac{1}{\mu_{hyd}(T)} + \frac{1}{\mu^{II}_{c,hyd}(\varphi,T)}\Bigg[\frac{\Gamma(1+\beta)}{(p\,t_{ref})^{\beta}} \\ & - \frac{\Gamma(1+\beta, p\,t_{tst})}{(p\,t_{ref})^{\beta}} + C\,\exp(-p\,t_{tst})\,\ln(1+B) + C\,\exp\left(\frac{p\,t_{tst}}{B}\right) \\ & \times G^{2,0}_{1,2}\left(\begin{smallmatrix}1\\0,0\end{smallmatrix}\middle|\,\frac{(1+B)\,p\,t_{tst}}{B}\right)\Bigg]\Bigg\}\,\mathbb{I}_{dev}\,,\end{aligned} \tag{56}$$

with the gamma function Γ and the Meijer G-function G. The Laplace–Carson transformed relaxation tensor follows, according to Eq. (55), from inversion of Eq. (56) yielding:

$$\begin{aligned}\mathbb{R}^{*,II}_{hyd}(p,\varphi,T) = {} & 3\,k_{hyd}(T)\mathbb{I}_{vol} + 2\Bigg\{\frac{1}{\mu_{hyd}(T)} + \frac{1}{\mu^{II}_{c,hyd}(\varphi,T)}\Bigg[\frac{\Gamma(1+\beta)}{(p\,t_{ref})^{\beta}} \\ & - \frac{\Gamma(1+\beta, p\,t_{tst})}{(p\,t_{ref})^{\beta}} + C\,\exp(-p\,t_{tst})\,\ln(1+B) + C\,\exp\left(\frac{p\,t_{tst}}{B}\right) \\ & \times G^{2,0}_{1,2}\left(\begin{smallmatrix}1\\0,0\end{smallmatrix}\middle|\,\frac{(1+B)\,p\,t_{tst}}{B}\right)\Bigg]\Bigg\}^{-1}\mathbb{I}_{dev}\,.\end{aligned} \tag{57}$$

Noting that the Laplace–Carson transformed constitutive laws of Eq. (54) are formally identical to those of linear elasticity, the upscaling of viscoelastic properties can be realized in terms of a quasi-elastic homogenization in the Laplace–Carson space. This strategy is known as the correspondence principle [13,14,83]. In this line, the three-step homogenization procedure for elastic material behavior of concrete given in Eqs. (3)–(6) is now adapted for the viscoelastic homogenization in the Laplace–Carson domain. Accordingly, the relaxation tensor of the creeping hydrates (57) enters the Laplace–Carson transformed relaxation tensor of the hydrate foam, such that the latter reads as

$$\begin{aligned}\mathbb{R}^*_{hf}(\xi,p,\varphi,T) = {} & \Bigg(f^{hf}_{por}(\xi)\,\mathbb{C}_{por} : \Big\{\mathbb{I} + \mathbb{P}^*_{sph}(p) : \Big[\mathbb{C}_{por} - \mathbb{R}^*_{hf}(\xi,p,\varphi,T)\Big]\Big\}^{-1} \\ & + f^{hf}_{hyd}(\xi)\int_{0}^{2\pi}\!\!\int_{0}^{\pi} \mathbb{R}^{*,II}_{hyd}(p,\varphi,T) : \Big\{\mathbb{I} + \mathbb{P}^*_{cyl}(p,\phi,\vartheta) \\ & : \Big[\mathbb{R}^{*,II}_{hyd}(p,\varphi,T) - \mathbb{R}^*_{hf}(\xi,p,\varphi,T)\Big]\Big\}^{-1}\frac{\sin\vartheta}{4\pi}\,\mathrm{d}\vartheta\mathrm{d}\phi\Bigg) \\ & : \Bigg(f^{hf}_{por}(\xi)\Big\{\mathbb{I} + \mathbb{P}^*_{sph}(p) : \Big[\mathbb{C}_{por} - \mathbb{R}^*_{hf}(\xi,p,\varphi,T)\Big]\Big\}^{-1}\end{aligned}$$

$$+ f_{hyd}^{hf}(\xi) \int_0^{2\pi}\!\!\int_0^{\pi} \left\{ \mathbb{I} + \mathbb{P}^*_{cyl}(p,\phi,\vartheta) : \left[\mathbb{R}^{*,II}_{hyd}(p,\varphi,T) - \mathbb{R}^*_{hf}(\xi,p,\varphi,T)\right] \right\}^{-1} \frac{\sin\vartheta}{4\pi}\, \mathrm{d}\vartheta \mathrm{d}\phi \Bigg)^{-1}, \tag{58}$$

and subsequently, the Laplace–Carson transformed relaxation tensors of cement paste and concrete follow as

$$\begin{aligned}\mathbb{R}^*_{cp}(\xi,p,\varphi,T) =& \Bigg(f^{cp}_{hf}(\xi)\,\mathbb{R}^*_{hf}(\xi,p,\varphi,T) \\ &+ f^{cp}_{cli}(\xi)\,\mathbb{C}_{cli} : \left\{ \mathbb{I} + \mathbb{P}^*_{sph}(p)\left[\mathbb{C}_{cli} - \mathbb{R}^*_{hf}(\xi,p,\varphi,T)\right] \right\}^{-1} \\ &+ f^{cp}_{slg}(\xi)\,\mathbb{C}_{slg} : \left\{ \mathbb{I} + \mathbb{P}^*_{sph}(p)\left[\mathbb{C}_{slg} - \mathbb{R}^*_{hf}(\xi,p,\varphi,T)\right] \right\}^{-1} \\ &+ f^{cp}_{lim}\,\mathbb{C}_{lim} : \left\{ \mathbb{I} + \mathbb{P}^*_{sph}(p)\left[\mathbb{C}_{lim} - \mathbb{R}^*_{hf}(\xi,p,\varphi,T)\right] \right\}^{-1} \Bigg) \\ &: \Bigg(f^{cp}_{hf}(\xi)\,\mathbb{I} + f^{cp}_{cli} \left\{ \mathbb{I} + \mathbb{P}^*_{sph}(p)\left[\mathbb{C}_{cli} - \mathbb{R}^*_{hf}(\xi,p,\varphi,T)\right] \right\}^{-1} \\ &+ f^{cp}_{slg}(\xi) \left\{ \mathbb{I} + \mathbb{P}^*_{sph}(p)\left[\mathbb{C}_{slg} - \mathbb{R}^*_{hf}(\xi,p,\varphi,T)\right] \right\}^{-1} \\ &+ f^{cp}_{lim} \left\{ \mathbb{I} + \mathbb{P}^*_{sph}(p)\left[\mathbb{C}_{lim} - \mathbb{R}^*_{hf}(\xi,p,\varphi,T)\right] \right\}^{-1} \Bigg)^{-1}, \end{aligned} \tag{59}$$

and

$$\begin{aligned}\mathbb{R}^*_{con}(\xi,p,\varphi,T) =& \Bigg(f^{con}_{cp}(\xi)\,\mathbb{R}^*_{cp}(\xi,p,\varphi,T) + \sum_j f^{con}_j\,\mathbb{C}_{agg,j} \\ &: \left\{ \mathbb{I} + \mathbb{P}^*_{sph}(p) : \left[\mathbb{C}_j - \mathbb{R}^*_{cp}(\xi,p,\varphi,T)\right] \right\}^{-1} \Bigg) : \Bigg(f^{con}_{cp}(\xi)\,\mathbb{I} \\ &+ \sum_j f^{con}_j \left\{ \mathbb{I} + \mathbb{P}^*_{sph}(p) : \left[\mathbb{C}_j - \mathbb{R}^*_{cp}(\xi,p,\varphi,T)\right] \right\}^{-1} \Bigg)^{-1}, \end{aligned} \tag{60}$$

with $\mathbb{P}^*_{cyl}(p)$ and $\mathbb{P}^*_{sph}(p)$ standing for the Laplace–Carson transformed Hill tensor of cylindrical and spherical inclusions, respectively [9], and where the volume fractions of the individual constituents inside their corresponding RVEs can be obtained by inserting Eq. (40) into Eqs. (16), (31), (32), (37), and (38) see also Figs. 7 and 8.

Eventually, the Laplace–Carson-transformed creep tensor function of concrete is determined from the inversion relation between the relaxation tensor and the creep tensor, given in Eq. (55). The corresponding tensor component $J_{1111}(\xi,p)$ represents hydration degree-specific Laplace–Carson transformed uniaxial creep functions of the isotropic material. When keeping the values for ξ, φ, and T fixed, the creep functions associated with Eq. (60) can be approximated in a very satisfactory fashion by functions with the creep modulus $E_{c,con}(\xi,\varphi,T)$ as fitting parameter, reading as

$$\begin{aligned} J^*_{con}(\xi,p,\varphi,T) =& \frac{1}{E_{con}(\xi,T)} + \frac{1}{E_{c,con}(\xi,\varphi,T)} \Bigg[\frac{\Gamma(1+\beta)}{(p\,t_{ref})^\beta} - \frac{\Gamma(1+\beta,p\,t_{tst})}{(p\,t_{ref})^\beta} \\ &+ C\,\exp(-p\,t_{tst})\,\ln(1+B) + C\,\exp\!\left(\frac{p\,t_{tst}}{B}\right) G^{2,0}_{1,2}\!\left(\left. {1 \atop 0,0} \right| \frac{(1+B)\,p\,t_{tst}}{B} \right) \Bigg], \end{aligned} \tag{61}$$

with the power-law exponent $\beta = 0.25$ and the transition time $t_{tst} = 32\,\mathrm{d}$. Eq. (61) can be back-transformed to the time domain analytically, as

$$\begin{aligned} &J_{con}(\xi,t-\tau,\varphi,T) \\ &= \frac{1}{E_{con}(\xi,T)} + \begin{cases} \dfrac{1}{E_{c,con}(\xi,\varphi,T)} \left(\dfrac{t-\tau}{t_{ref}}\right)^{\beta} & \ldots \begin{cases} t \geq \tau\,, \\ t \leq \tau + t_{tst}\,, \end{cases} \\ \dfrac{C}{E_{c,con}(\xi,\varphi,T)} \ln\!\left(1 + B\,\dfrac{t-\tau}{t_{tst}}\right) & \ldots\ t \geq \tau + t_{tst}\,, \end{cases} \end{aligned} \tag{62}$$

see the Appendix for corresponding details.

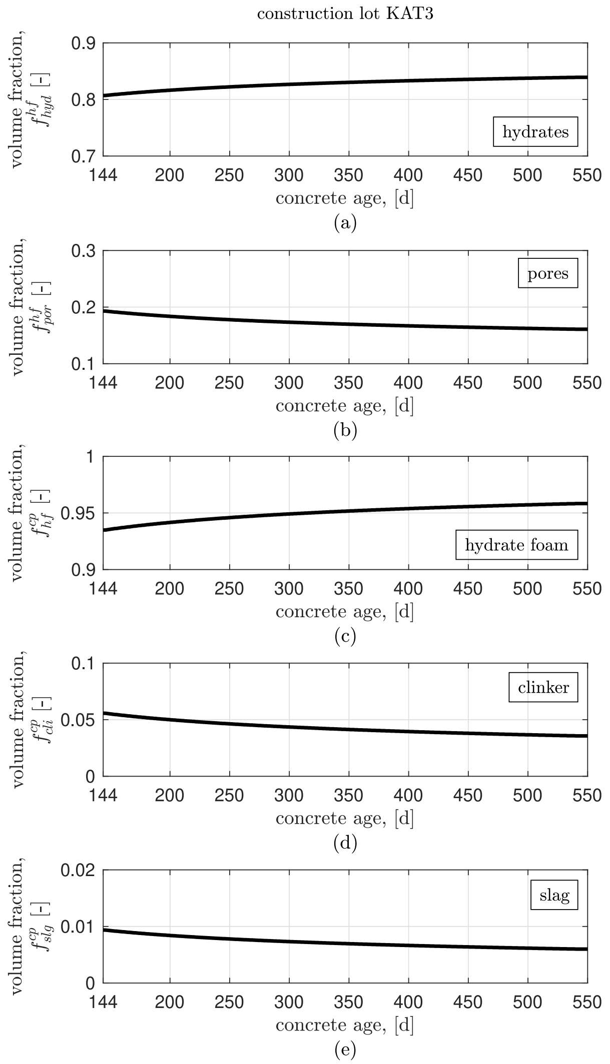

Fig. 7. Evolution of RVE-specific volume fractions of the individual constituents inside the concrete tested at KAT3 construction lot [29]: (a) hydrates and (b) pores in the RVE of hydrate foam; (c) hydrate foam, (d) clinker, and (e) slag in the RVE of cement paste.

4.3. Consideration of aging effects on concrete creep

The hydration degree of the concrete specimens increased continuously during the creep tests, see Fig. 6. This hydration-dependent aging motivates the use of a model for aging viscoelasticity [21], in which the classical convolution integral of Boltzmann shown e.g. in Eq. (51) is substituted by a hydration-degree-dependent convolution integral relating the strain rate (rather than the total strain) to the stress rate $\dot{\boldsymbol{\sigma}}$, in the following form:

$$\boldsymbol{d}(t) \quad = \quad \int_{-\infty}^{t} \mathbb{J}_d\big(\xi(t), t-\tau\big) \,:\, \dot{\boldsymbol{\sigma}}(\tau)\, \mathrm{d}\tau\,, \tag{63}$$

where $\boldsymbol{d}(t)$ stands for the Eulerian strain rate tensor, $\boldsymbol{d} \approx \dot{\boldsymbol{\varepsilon}}$ in the case of linearized strains, and where $\mathbb{J}_d$ refers to the creep rate function tensor [25], which depends on the current hydration degree. $\mathbb{J}_d$ can be approximated by the partial time derivative of a classical creep tensor function $\mathbb{J}$ describing a non-aging material associated with a particular hydration degree ξ [21], according to

$$\mathbb{J}_d\big(\xi(t), t-\tau\big) \approx \frac{\partial}{\partial t}\mathbb{J}\big(\xi(t), t-\tau\big)\,. \tag{64}$$

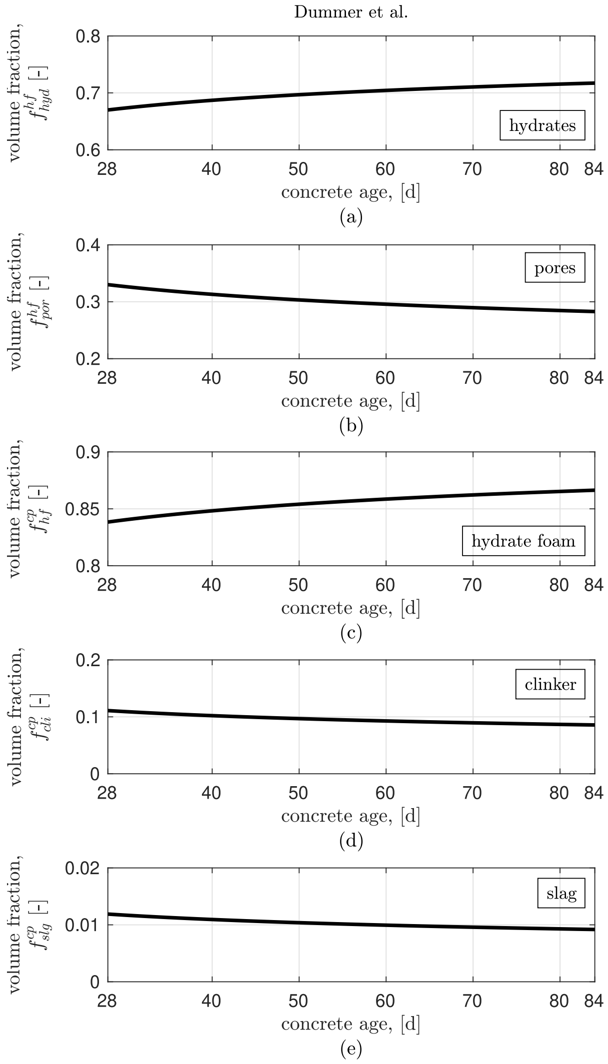

Fig. 8. Evolution of RVE-specific volume fractions of the individual constituents inside the concrete tested by Dummer et al. [30]: (a) hydrates and (b) pores in the RVE of hydrate foam; (c) hydrate foam, (d) clinker, and (e) slag in the RVE of cement paste.

As regards the macroscopic creep function (62), hydration-dependent aging refers to the evolution of the elastic Young's modulus and the creep modulus, $E(\xi(t),T)$ and $E_c(\xi(t),\varphi,T)$, respectively, where t refers to the material age. The uniaxial creep rate function J_d is then approximated as the partial time derivative of Eq. (62), as

$$J_d\big(\xi(t),t-\tau,\varphi,T\big) = \frac{\partial}{\partial t} J_{con}\big(\xi(t),t-\tau,\varphi,T\big) = \tag{65}$$
$$= \frac{\delta(t-\tau)}{E_{con}\big(\xi(t),T\big)} + \begin{cases} \dfrac{H(t-\tau)}{E_{c,con}\big(\xi(t),\varphi,T\big)}\,\dfrac{\beta}{t_{ref}}\left(\dfrac{t-\tau}{t_{ref}}\right)^{\beta-1} & \ldots \begin{cases} t \geq \tau\,, \\ t \leq \tau + t_{tst}\,, \end{cases} \\ \dfrac{H(t-\tau)\,C\,B}{E_{c,con}\big(\xi(t),\varphi,T\big)}\,\dfrac{1}{\left[t_{tst}+B\,(t-\tau)\right]} & \ldots\ t \geq \tau + t_{tst}\,, \end{cases}$$

where $\delta(t-\tau)$ refers to the Dirac delta function, and $H(t-\tau)$ denotes the Heaviside function.

The viscoelastic strains occurring during the creep tests are finally obtained by inserting Eqs. (64) and (65) into the uniaxial form of Eq. (63), and integrating the result over time, as [21,25]

$$\varepsilon(t) = \int\limits_{\zeta=-\infty}^{\zeta=t}\ \int\limits_{\tau=-\infty}^{\tau=\zeta} J_d\big(\xi(\zeta),\zeta-\tau,\varphi,T\big) : \frac{\partial}{\partial\tau}\sigma(\tau)\,\mathrm{d}\tau\,\mathrm{d}\zeta\,, \tag{66}$$

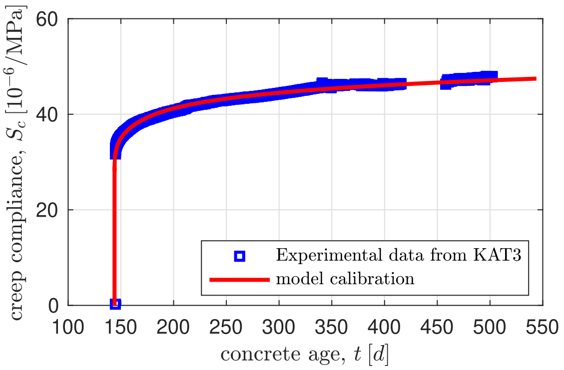

Fig. 9. Creep of concrete under uniaxial compression: experimentally determined creep compliance from [29], see the blue data points and Fig. 1, and micromechanics-predicted compliance according to Eq. (67), based on $\tilde{\mu}^{II}_{c,hyd} = 10.46\,\text{GPa}$, see the red solid lines. (For interpretation of the references to color in this figure legend, the reader is referred to the web version of this article.)

where ζ is a time integration variable for the summation of strain rates. Normalizing these aging-affected strains yields a compliance

$$S\big(t;\tilde{\mu}^{II}_{c,hyd}\big) = \frac{\varepsilon\big(t;\tilde{\mu}^{II}_{c,hyd}\big)}{\sigma}\,, \tag{67}$$

where the dependence of the creep compliance, via $E_{c,con}$, on the shear creep modulus $\tilde{\mu}^{II}_{c,hyd}$ is emphasized.

4.4. Identification of the shear creep modulus of hydrates made from CEM II/A-S 52.5 N

The micromechanical analysis leading to Eq. (62) shows that the hydrates are the only creeping constituent inside concrete, and that the creep behavior of the investigated concretes can be determined from the creep exponent $\beta = 0.25$ and the shear creep modulus of hydrates made from CEM II/A-S 52.5 N, $\tilde{\mu}^{II}_{c,hyd}$, prevailing at a temperature of 20°C and a relative humidity of 100%. The latter is herein identified by minimizing the error between the model-predicted creep compliance, $S\big(\tilde{\mu}^{II}_{c,hyd}\big)$, calculated according to Eqs. (65)–(67), together with Eqs. (57)–(60), the volume fractions (16), (31), (32), (37), (38), the hydration degrees given in Fig. 6 and the stress levels, temperature and relative humidity given in Table 3; and the creep compliance obtained during the creep experiments performed at KAT3, S_{exp}, see Fig. 1. Mathematically, this minimization process reads as:

$$\mathcal{R} = \sqrt{\frac{1}{N_K}\sum_{n=1}^{N_K}\Big[S\big(\tilde{\mu}^{II}_{c,hyd};t_n\big) - S_{\exp}(t_n)\Big]^2} \rightarrow \min\ \Rightarrow\ \tilde{\mu}^{II}_{c,hyd}\,, \tag{68}$$

where $N_K = 2471$ is equal to the number of measurements taken during the creep test, and where $t_n = n \times 1\,\text{h}$ for the initial 64 days, followed by an extension of the time span between two successive readings to six hours [29]. The elastic response of the specimen at every time instant is determined from Eq. (39), and ranges from $E_{con} = 37.8\,\text{GPa}$ at the beginning of the test to $E_{con} = 38.6\,\text{GPa}$ at its end. The optimal value for the shear creep modulus of hydrates made from CEM II/A-S 53.5 N is thus obtained as

$$\tilde{\mu}^{II}_{c,hyd} = 10.46\,\text{GPa}\,. \tag{69}$$

This value allowed for a satisfactory reproduction of the experimental data from creep testing at KAT3, see Fig. 9.

4.5. Model validation: Predicting creep of concrete made from CEM II/AM (S-L) 42.5 N [30]

The micromechanical model of Eqs. (56)–(60) and (65)–(67) is now used to predict experimental data from creep tests on concrete made

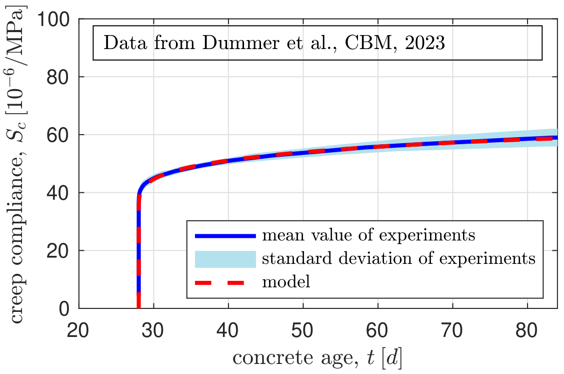

Fig. 10. Prediction of creep test data from Dummer et al. [30]. The red solid line refers to the predictions based on Eq. (67), while the blue solid line and the light blue shaded area refer to the mean value and standard deviation of the experimental data. (For interpretation of the references to color in this figure legend, the reader is referred to the web version of this article.)

from CEM II/AM (S-L) 42.5 N and limestone aggregates [30]. The shear creep modulus of hydrates at the tested conditions, $\mu^{II}_{c,hyd}(\varphi = 97\%, T = 20°\text{C})$, is obtained from (50) evaluated for $\varphi = 97\%$ and $T = 20°\text{C}$, together with (69). This temperature-activated and relative humidity-informed shear creep modulus is then used as an input for the micro-viscoelastic model according to Eqs. (65)–(67), together with Eqs. (57)–(60), the volume fractions (16), (31), (32), (37), (38), the hydration degrees given in Fig. 6 and the stress levels, temperature and relative humidity given in Table 3. This model predicts, with remarkable accuracy, both the short-term and the long-term creep behavior observed in the tests performed by Dummer et al. [30], as quantified by the weighted mean of absolute values of relative errors between predicted and measured compliance values, according to

$$\mathcal{R}_W = \sum_{n=1}^{N_D} \frac{\left|S(t_n) - S_{exp}(t_n)\right|}{S_{exp}(t_n)} \frac{t_n - t_{n-1}}{t_{N_D} - t_0} = 0.3\%\,, \tag{70}$$

where $N_D = 59$ refers to the total amount of time instants where measurements are available, $(t_n - t_{n-1})$ refers to the weight of the error obtained at the time instant t_n, while $S(t_n)$ and $S_{exp}(t_n)$ refer to the model-predicted and the experimentally obtained compliance at the time instant t_n, respectively, see Fig. 10. The corresponding coefficient of determination is also very high, namely $R^2 = 0.9965$. Notably, both tests were performed at different temperatures, relative humidities, and maturities, while also lasting for a different amount of time. This shows the robustness of the proposed creep model, which is able to account for the effects of thermal activation, relative humidity, and aging. Furthermore, both experiments were performed on different types of slag-based CEM II cement pastes. This indicates that the shear creep modulus from Eq. (69) is valid for both cement pastes, and may hence be applicable for a wide variety of mature slag-based CEM II cement pastes.

5. Discussion

The concretes used for the two investigated tests present very different microstructural properties at different scales of observation. As regards the concrete of the KAT3 test [29], the cement type CEM II/A-S 52.5 N was used, where “A-S” stands for a cement including slag with a mass fraction ranging from 6% to 20%. Furthermore, the test was started at an age of 144 days and lasted for over 356 days, referring to a relatively mature cement with hydration degrees ranging from 85% to 90%. The aggregates interacting with the cement paste were composed of a mixture of dolomite, limestone, granite, quarzite, basalt, and diabase. The creep tests were further performed at a temperature of 21°C, and a relative humidity of 72%. As regards the concrete of the test by Dummer et al. [30], the cement type CEM II/AM (S-L) 42.5 N was used, where “AM (S-L)” stands for a cement including a mixture of slag and limestone with a mass fraction ranging from 12% to 20%. Furthermore, the test was started at an age of 28 days and lasted for 56 days, referring to a less mature cement with a hydration degree ranging from 68% to 75%. The aggregates interacting with the cement paste were composed of limestone only. The creep tests were further performed at a temperature of 20°C, and a relative humidity of 97%.

Despite the evident differences in the compositions of the two concretes and the conditions under which they were tested, it is remarkable that *the same* shear creep modulus of CEM II hydrates explained *both* tests very accurately. This supports the interpretation that the found shear creep modulus (69) is mixture- and maturity-independent.

The CEM II hydrates exhibit a much more pronounced creep activity than those made from CEM I, as quantified by a shear creep modulus that is, by a factor of two, smaller. This enhanced creep activity can be explained by pozzolanic hydration reactions of slag in CEM II, where non-creeping portlandite is consumed, leading to the production of additional, creep-active, calcium-silicate-hydrates [84]. It is this increased amount of C-S-H in the hydration products of the mixtures which leads to an increased creep response.

This increased creep response is quantified in terms of a largely invariant shear creep modulus of CEM II hydrates, holding for two different concretes and for a range of hydration degrees; and this appears as very remarkable, given the pronouncedly complex nature of hydration products. Strictly speaking, hydrates do not dispose over invariant physical properties, but undergo significant densification during hydration, as evidenced by proton nuclear magnetic resonance (^{1}H NMR) tests on both white cement pastes [85–87] and on slag-blended cement pastes [39,88], and the underlying chemical processes can be suitably described by mathematical models resting on precipitation, rather than overall hydration, quantities, such as the precipitation space or the precipitation degree [40,89,90]. In addition, the water bound in these hydration products is surprisingly mobile, migrating between interlayer, gel, and capillary spaces, not only upon temperature changes [91,92], but also due to external mechanical loading [93]. All this seems at odds with the herein identified fairly invariant hydrate shear creep modulus. Still, the latter can be explained by the quite high maturity of the material systems investigated herein, with hydration degrees ranging between 0.68 and 0.90: At this level of maturity, densification and gel pore water migration effects are of only secondary importance. More precisely, in this maturity interval, both white CEM I hydrates and slag-based CEM II hydrates densify by only some 5% in cement paste with an initial water-to-cement mass ratio of 0.44 [40,89]. Still, for early age investigations, a dedicated poro-micromechanical approach [54], which not only resolves the hydrate phases into finer constituents such as gel pores and solid C-S-H, but also considers the aforementioned mathematically modeled hydrate densification process, may be adopted, in order to account for hydrate densification processes governing mechanical properties and to get access to gel pore pressures driving transport phenomena. However, this is beyond the scope of the present paper.

The developed model was able to reproduce and predict experimental data of CEM II concrete creep with a very high level of accuracy, based on mixture and hydration degree-specific concrete creep moduli, appearing in Eqs. (61) and (62), depicted in Fig. 11. The explicit consideration of microstructural properties of the investigated material systems, as well as the environmental conditions of the tests, yields a robust micromechanical model for temperature-activated, moisture-sensitive, short-to-long term aging creep of concrete that can be used for a variety of different conditions and concrete compositions. This way, improved predictions of the creep behavior of cementitious materials can be achieved, leading to optimized mix designs that may be adapted to fulfill specific performance requirements in the construction sector.

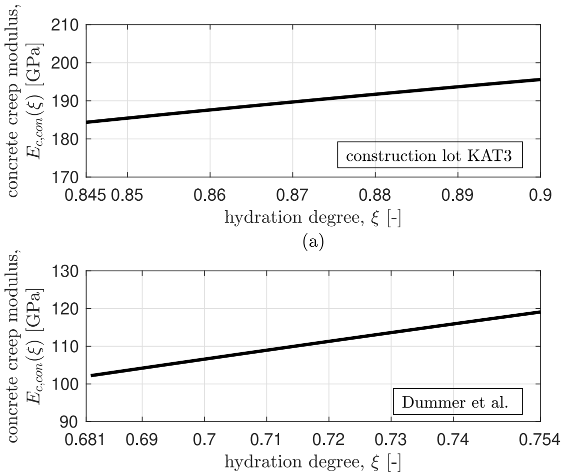

(a)

(b)

Fig. 11. Evolution of the concrete creep modulus, $E_{c,con}$, in CEM II concretes tested (a) in KAT3 construction lot [29] and (b) by Dummer et al. [30].

Table 8
Input values for the four parametric analyses concerning the concretes used at the KAT3 construction lot [29] and by Dummer et al. [30].

KAT3 construction lot			
m_{slg}/m_{cli} [%]	f_{agg}^{con} [%]	φ [%]	T [°C]
5–25	71.6	72	21
15	65.0–75.0	72	21
15	71.6	40–100	21
15	71.6	72	5–35
Concrete investigated by Dummer et al.			
m_{slg}/m_{cli} [%]	f_{agg}^{con} [%]	φ [%]	T [°C]
6–14	71.3	97	20
10	65.0–75.0	97	20
10	71.3	40–100	20
10	71.3	97	5–35

The developed powerful micromechanical model allows us to quantify the impact of compositional and environmental quantities on the creep behavior of CEM II material systems. We do this by means of a parametric analysis where each of four key quantities plays the role of an independent variable. These independent variables are, one by one, mapped onto the creep compliance (which is the dependent parameter), while keeping all other compositional and environmental quantities, and in particular so the initial water-to-cement mass ratio, constant. As the four independent variables we choose: (i) the initial slag-to-clinker mass ratio, (ii) the volume fraction of aggregates in a volume of concrete, (iii) the temperature, and (iv) the relative humidity.

In more detail, for investigation of the impact of slag content in CEM II/A-S 52.5 N as used at the KAT3 construction lot, we resort to the European regulation for slag-based CEM II binders [3], so that we vary the initial slag-to-clinker mass ratio between 5% and 25%, while keeping the initial water-to-cement mass ratio constant at 0.44. Accordingly, any variation of the initial slag-to-clinker mass ratio is accompanied by a variation of the initial water-to-clinker mass ratio according to

$$\frac{m_{\mathrm{H_2O}}}{m_{cli}} = 0.44 \times \left(1 + \frac{m_{slg}}{m_{cli}}\right). \tag{71}$$

On the other hand, for investigation of the impact of slag content in CEM II/AM (S-L) 42.5 N as used by Dummer et al. [30], the European regulation [3] allows the initial ratio between the sum of the slag and limestone masses and the clinker mass to range from 14% to 25%, while the initial slag-to-limestone mass ratio remains unspecified. This motivates us to keep the initial slag-to-limestone mass ratio constant at the actual value, namely at $m_{slg}/m_{lim} = 1$, while investigating the effect of initial slag-to-clinker mass ratios ranging from 6% to 14%, with a step size of 4%. In order to keep the initial water-to-cement mass ratio constant at 0.44, the initial water-to-clinker mass ratio is updated as follows:

$$\frac{m_{\mathrm{H_2O}}}{m_{cli}} = 0.44 \times \left(1 + 2\,\frac{m_{slg}}{m_{cli}}\right). \tag{72}$$

All other micromechanical properties of the investigated concretes remain the same. This includes the creep properties of the hydrates, the concrete-specific evolution of the hydration degree throughout the simulated creep tests, the volume fractions of the aggregates in a volume of concrete, the temperatures, and the relative humidities, see also the first data line in the upper and lower portions of Table 8, respectively. Under these conditions, the effect of the slag content on the creep properties is more pronounced for the concrete tested by Dummer et al. [30], as it was tested at a lower hydration degree where the volume fraction of slag is correspondingly larger. Yet, also for this concrete the investigated slag content variations do not alter the creep compliance by more than ±3%, with increasing slag content amplifying creep, see Fig. 12(b). By comparison, at a higher hydration degree, as experienced in the concrete tested at the KAT3 construction lot [29], the variations on slag content are small, and hence, also the effect on creep is almost negligible, see Fig. 12(a).

In order to assess the impact of aggregate content on the creep of concrete, the volume fraction of the aggregates in a volume of concrete is varied from 65% to 75%, with a step size of 2.5%. This requires the following update of the volume fraction of the cement paste in a volume of concrete:

$$f_{cp}^{con} = 1 - f_{agg}^{con}. \tag{73}$$

All other micromechanical properties of the studied concretes remain the same. This includes the creep properties of the hydrates, the concrete-specific evolution of the hydration degree throughout the simulated creep tests, the initial slag-to-clinker mass ratios, the temperatures, and the relative humidities, see also the second data line of the upper and lower portions of Table 8, respectively. The considered variation of the aggregate content implies a variation in creep compliance of 26% and 27%, with increasing aggregate content attenuating the concrete creep, see Figs. 13(a) and 13(b), respectively.

In order to assess the impact of temperature on the isothermal creep of concrete, the temperature is varied from 5°C to 35°C, with a step size of 5°C. Temperature rise implies increase of creep compliance of the hydrates according to Eq. (50). With all other micromechanical properties remaining the same, see the third data line in the upper and lower portions of Table 8, respectively, the hydrate compliance variations are upscaled to the concrete scale, leading there to creep compliance variations of 37% and 39%, see Figs. 14(a) and 14(b), respectively. Similarly, hydrate creep is governed by the relative humidity, see again Eq. (50). This becomes evident when varying the relative humidity from 40% to 100%, with a step size of 10%, while keeping all other micromechanical properties constant, see the fourth data line of the upper and lower portions of Table 8. Corresponding creep compliance variations at the concrete level amount to 45% and 36%, respectively, see Figs. 15(a) and 15(b), respectively.

All these model predictions rest on the evolution of the hydration degree, as assessed through Eq. (39), i.e., on the fib Model Code [71]. Hence, the question arises whether the determination of the hydration degree from the fib Model Code [71] and the micromechanical model of Pichler and Hellmich [26] is precise enough, when compared to hydration degree determination based on calorimetric tests [70,94–96]. In this context, the following is noteworthy: Ausweger et al. [97] showed that the fib Model Code [71] can satisfactorily predict the evolution of the elastic Young's modulus of CEM II concretes under isothermal conditions for ages larger than 7 days. This qualifies the fib

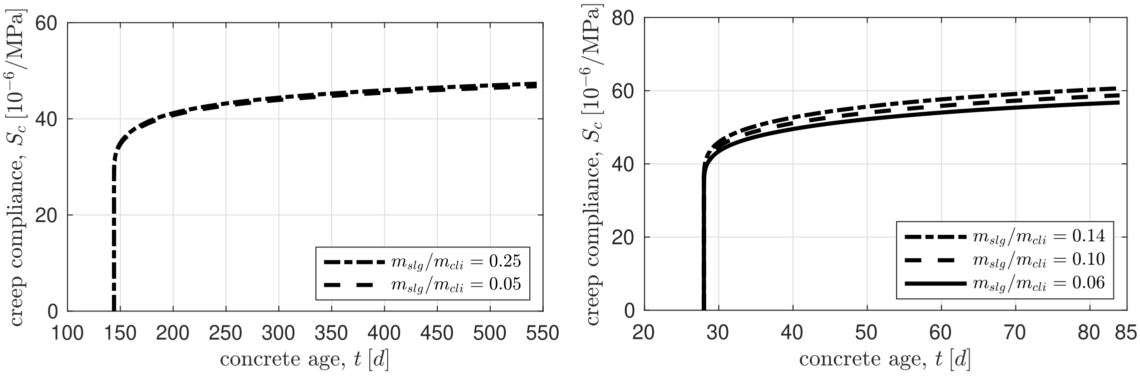

(a)

(b)

Fig. 12. Parametric analysis: influence of the slag content of cement on the creep of concrete: (a) CEM II/A-S 52.5 N-based concrete tested at KAT3 [29], and (b) CEM II/AM (S-L) 42.5 N-based concrete of Dummer et al. [30].

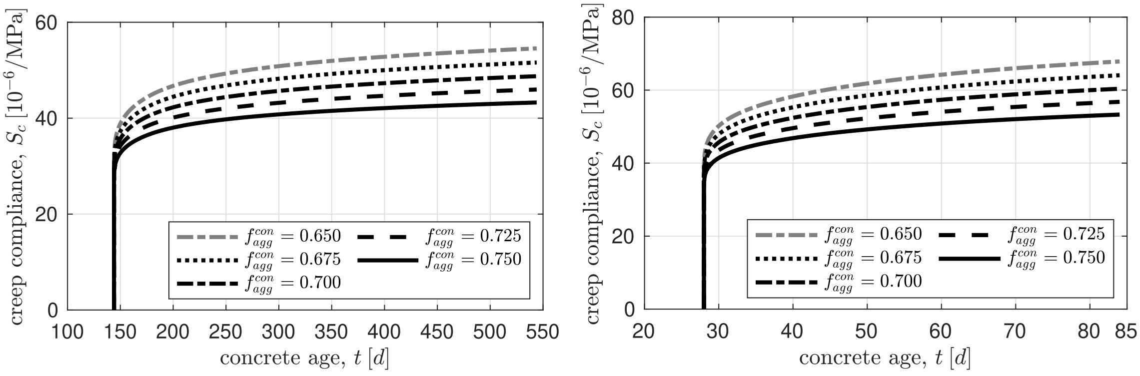

(a)

(b)

Fig. 13. Parametric analysis: influence of the aggregate content on the creep of concrete: (a) CEM II/A-S 52.5 N-based concrete tested at KAT3 [29], and (b) CEM II/AM (S-L) 42.5 N-based concrete of Dummer et al. [30].

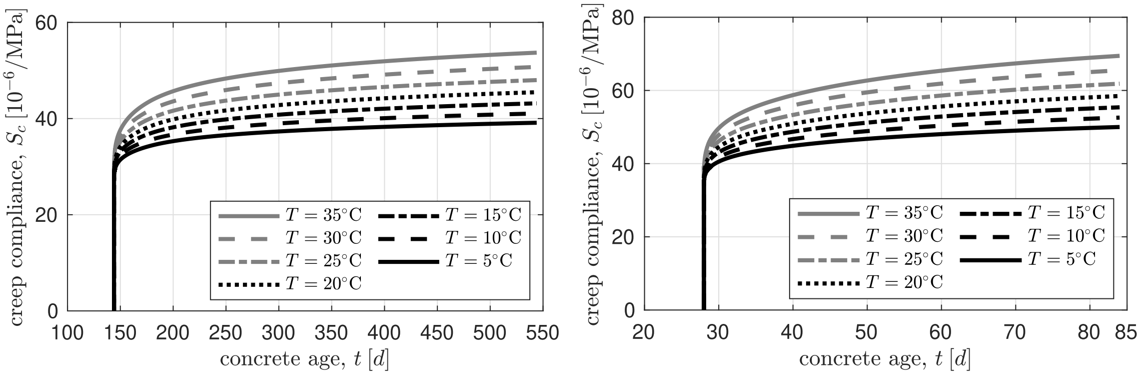

(a)

(b)

Fig. 14. Parametric analysis: influence of the temperature on the creep of concrete: (a) CEM II/A-S 52.5 N-based concrete tested at KAT3 [29], and (b) CEM II/AM (S-L) 42.5 N-based concrete of Dummer et al. [30].

Model Code, in addition to calorimetric tests, as a means for accessing hydration evolutions in CEM II concretes. Actually, the fib Model Code gives access to evolutions at high and very high maturation states, while calorimetric tests can hardly provide hydration evolutions for ages larger than three weeks [94,95]. For the transition from elastic Young's modulus to hydration degree, an experimentally validated micromechanical model is required: for the present application, we use the model of Pichler and Hellmich [26].

One may also ask whether the currently adopted modeling approach is restricted to isothermal conditions at 20°C. The corresponding answer is “no”: In case of isothermal conditions at temperatures different from 20°C, or of non-isothermal conditions expressed through different temperature values associated with different time intervals Δt_i, the fib

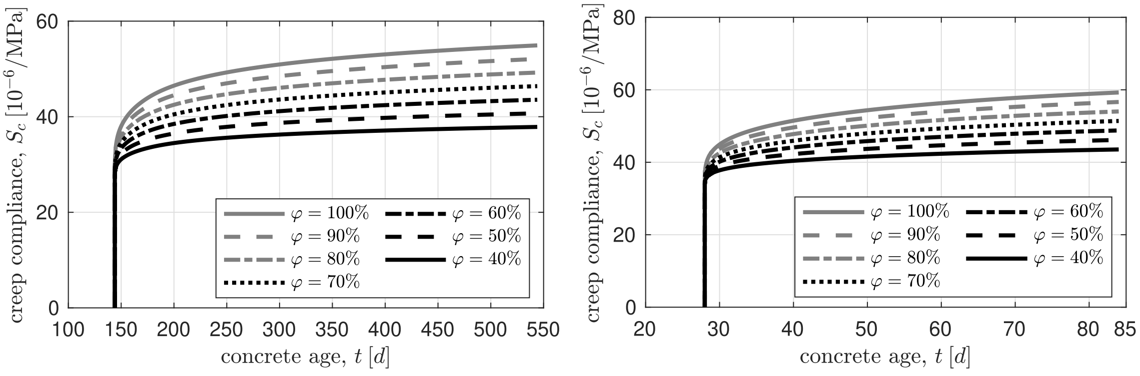

(a)

(b)

Fig. 15. Parametric analysis: influence of the relative humidity on the creep of concrete: (a) CEM II/A-S 52.5 N-based concrete tested at KAT3 [29], and (b) CEM II/AM (S-L) 42.5 N-based concrete of Dummer et al. [30].

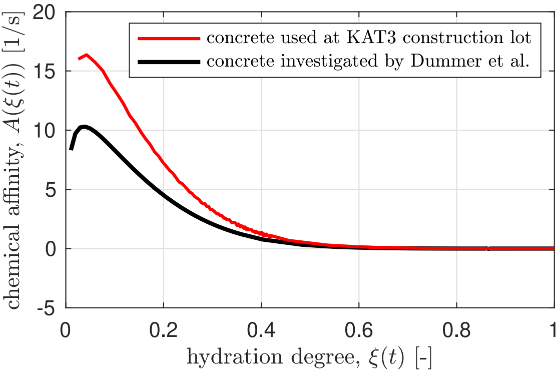

Fig. 16. Chemical affinity for the concrete used at the KAT3 construction lot [29], see the red solid line, and for the concrete investigated by Dummer et al. [30], see the black solid line. (For interpretation of the references to color in this figure legend, the reader is referred to the web version of this article.)

Model Code [71] refers to the concept of an equivalent age t_{eq}: The latter, rather than to the actual age, enters the elasticity evolution approximation of Eq. (39). Thereby, the equivalent age is computed from [71]

$$t_{eq} = \sum_{i=1}^{n} \Delta t_i \exp\left[13.65 - \frac{4000}{273 + T(\Delta t_i)}\right], \text{ with } T \text{ given in °C.} \tag{74}$$

Eq. (74) gives access to the temperature-dependent "equivalent age reached after 28 days". The elastic Young's modulus measured at 28 days would then be associated to the aforementioned equivalent age, which, rather the real age, enters Eq. (39). This allows for determination of $E_{con,28d}$. By example, considering that the KAT3-experiment was realized isothermally at 21 °C rather than 20 °C, the equivalent age reached at 144 days amounts to 151 days. Inserting this equivalent age, together with the 144-day elastic Young's modulus of 37.8 GPa, into Eq. (39) allows one to compute $E_{con,28d} = 35.71$ GPa. Once the value for $E_{con,28d}$ is known, the hydration degree can be again determined from Eq. (40). Such an access to the evolution of the hydration degree over time also allows for determination of the chemical affinity function governing an Arrhenius-type description of the hydration process, through [68]

$$\tilde{A}(t) = \dot{\xi}(t) \exp\left(\frac{E_a}{RT}\right), \tag{75}$$

where $E_a = 33260$ J/mol is the activation energy [70,90,98], see Fig. 16 for the mixtures investigated in the present paper. The latter function allows for thermochemomechanical anaylses of concrete structures [22,99]. Further refinement of our approach towards concrete kinetics approximation may involve the determination of the chemical affinity from calorimetric tests [68–70], or dedicated strength tests performed at different ages [98]. Such tests are currently not available for the CEM II concretes reported here; and they go beyond the scope of the present paper.

As a further limitation of the present approach, one may note the experimental validation being restricted to uniaxial creep tests. This limitation simply arises from the absence of biaxial and triaxial creep tests for slag-based CEM II concretes; while such tests have been reported for concretes based on ordinary Portland cement [100–102]. Obviously, this motivates additional experimental activities to be undertaken in the future.

6. Conclusion

The following conclusions are drawn:

- The identified shear creep modulus of hydrates made from CEM II was shown to reproduce the behavior of two microstructurally distinct concretes very accurately. This corroborates that the identified modulus may be taken as a mixture- and maturity-independent property, which is representative of the short-to-long term creep behavior of slag-based CEM II concretes.
- Hydrates made from slag-based CEM II cement paste exhibit much more pronounced creep than those made from CEM I, as quantified by a shear creep modulus of CEM II hydrates that is by a factor of two smaller than those from CEM I. This increased creep activity can be explained by the consumption of non-creeping portlandite to produce additional creeping CSH as a result of the pozzolanic hydration reaction of slag.
- Concrete made from slag-based CEM II is noted to be especially suitable for structures under displacement-controlled conditions, e.g. for the production of tunnel linings, because the larger creep-activation readily implies a faster relaxation of stresses.
- A robust and flexible micromechanical model for temperature-activated, moisture-sensitive, short-to-long term aging creep of concrete was developed, leading to very accurate predictions of the creep behavior of different mature CEM II cementitious materials.

CRediT authorship contribution statement

Maximilian Sorgner: Writing – original draft, Validation, Software, Investigation, Formal analysis. **Rodrigo Díaz Flores:** Writing – original

draft, Validation, Investigation. **Bernhard Pichler:** Writing – review & editing, Supervision, Methodology, Funding acquisition. **Thomas Pilgerstorfer:** Investigation, Data curation. **Bernd Moritz:** Investigation, Funding acquisition, Data curation. **Christian Hellmich:** Writing – review & editing, Writing – original draft, Supervision, Methodology, Funding acquisition, Conceptualization.

Acknowledgments

The authors gratefully acknowledge project FFG-COMET, Austria No. 882504 “Rail4Future: Resilient Digital Railway Systems to enhance performance”.

Appendix. Back-transformation of the point-wisely resolved *nonaging* uniaxial creep function of concrete from the laplace–carson space into the time domain

Key to the relevance of Eq. (61) for the precise description of concrete creep in the Laplace–Carson domain is the similarity of creep functions at the hydrate scale and the concrete scale, as stress redistributions between the creeping hydrate phases and the purely elastic cement particles and aggregates are virtually absent [55]. Since the mathematical structure of Eq. (61) is essentially that of Eq. (56), the back-transformation of Eq. (61) into the time domain is simply an expression mimicking the creep function which was originally adopted for the creep of the hydrate phases, i.e., Eqs. (42) and (43). This expression is given as Eq. (62). The only unknown in Eq. (61) is the creep modulus of concrete, $E_{c,con}$. It is identified such that Eq. (61) best reproduces the point-wisely computed solution of $J^*_{con}(\xi,p,\varphi,T)$, see Fig. 17 for the virtually perfect performance of Eq. (61). The corresponding mean relative fitting error is as low as 0.0061 (absolute errors between individual creep function values and values of the fitting function divided by average of LC-creep values), with a coefficient of determination reaching impressive 99.99%.

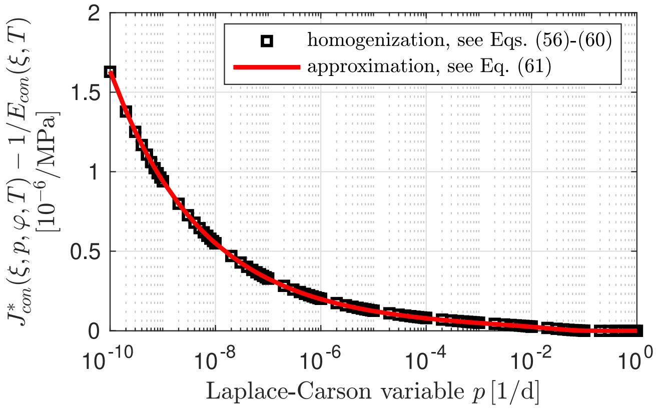

Fig. 17. Point-wisely resolved Laplace–Carson transformed homogenized nonaging uniaxial creep function of the KAT3-concrete with $\xi = 0.845$, $\varphi = 72\%$, and $T = 21°\text{C}$, see the black symbols, and its approximation by means of Eq. (61) yielding $E_{c,con} = 185.2\,\text{GPa}$, see the red graph. (For interpretation of the references to color in this figure legend, the reader is referred to the web version of this article.)

List of symbols

$\tilde{A}$	Chemical affinity
B	Dimensionless constant
C	Dimensionless constant
$\mathbb{C}_{blt}$	Elastic stiffness tensor of basalt
$\mathbb{C}_{dbs}$	Elastic stiffness tensor of diabase
$\mathbb{C}_{dol}$	Elastic stiffness tensor of dolomite
$\mathbb{C}_{grt}$	Elastic stiffness tensor of granite
$\mathbb{C}_{lim}$	Elastic stiffness tensor of limestone
$\mathbb{C}_{qzt}$	Elastic stiffness tensor of quarzite
$\mathbb{C}_{cli}$	Elastic stiffness tensor of clinker
$\mathbb{C}_{con}$	Elastic stiffness tensor of concrete
$\mathbb{C}_{cp}$	Elastic stiffness tensor of cement paste
$\mathbb{C}_{hyd}$	Elastic stiffness tensor of hydrates
$\mathbb{C}_{hf}$	Elastic stiffness tensor of hydrate foam
$\mathbb{C}_{lim}$	Elastic stiffness tensor of limestone
$\mathbb{C}_{por}$	Elastic stiffness tensor of pores
$\mathbb{C}_{slg}$	Elastic stiffness tensor of slag
C_{ijkl}	Component of the elastic stiffness tensor $\mathbb{C}$
D	Characteristic length of the dimension or loading of a structure built from the material defined on a RVE
$\mathbb{D}_{con}$	Elastic compliance tensor of concrete
D_{ijkl}	Component of the elastic compliance tensor $\mathbb{D}$
$\boldsymbol{d}$	Eulerian strain rate tensor
d	Characteristic length of inhomogeneities within a RVE
E_a	Activation energy of hydration
E_{hyd}	Elastic Young’s modulus of hydrates
E_{con}	Elastic Young’s modulus of concrete
$E_{con,28\text{d}}$	28-day elastic Young’s modulus of concrete
$E_{con,144\text{d}}$	144-day elastic Young’s modulus of concrete
$E_{c,con}$	Creep modulus of concrete
E_{hyd}	Elastic Young’s modulus of CEM I hydrates
F	Piecewisely defined function
f^{hf}_{hyd}	Volume fraction of hydrates in the RVE of hydrate foam
f^{hf}_{por}	Volume fraction of pores in the RVE of hydrate foam
f^{cp}_{cli}	Volume fraction of clinker in the RVE of cement paste
f^{cp}_{slg}	Volume fraction of slag in the RVE of cement paste
f^{cp}_{lim}	Volume fraction of limestone in the RVE of cement paste
$f^{cp}_{\text{H}_2\text{O}}$	Volume fraction of water in the RVE of cement paste
f^{cp}_{air}	Volume fraction of air in the RVE of cement paste
f^{cp}_{por}	Volume fraction of pores in the RVE of cement paste
f^{cp}_{hyd}	Volume fraction of hydrates in the RVE of cement paste
f^{cp}_{hf}	Volume fraction of hydrate foam in the RVE of cement paste
f^{cp}_{reac}	Volume fraction of reactants in the RVE of cement paste
f^{reac}_{cli}	Volume fraction of clinker in the RVE of reactants
f^{reac}_{slg}	Volume fraction of slag in the RVE of reactants
f^{con}_{cp}	Volume fraction of cement paste in the RVE of concrete
f^{con}_{agg}	Volume fraction of aggregates in the RVE of concrete
f^{con}_{blt}	Volume fraction of basalt in the RVE of concrete

f_{dbs}^{con}	Volume fraction of diabase in the RVE of concrete
f_{dol}^{con}	Volume fraction of dolomite in the RVE of concrete
f_{grt}^{con}	Volume fraction of granite in the RVE of concrete
f_{lim}^{con}	Volume fraction of limestone in the RVE of concrete
f_{qzt}^{con}	Volume fraction of quarzite in the RVE of concrete
$f_{c,28}$	28-day uniaxial compressive strength of concrete
$f^*(p)$	Laplace–Carson transform of any time dependent function $f(t)$
G	Meijer G-function
$\mathbb{I}$	Fourth-order identity tensor
$\mathbb{I}_{vol}$	Volumetric part of the fourth-order identity tensor
$\mathbb{I}_{dev}$	Deviatoric part of the fourth-order identity tensor
$\mathbb{J}$	Non-aging creep tensor function
$\mathbb{J}^*$	Laplace–Carson-transformed creep tensor function
$\mathbb{J}_{hyd}$	Universal isochoric non-aging creep tensor function of CEM I hydrates
$\mathbb{J}_{hyd}^{II}$	Universal isochoric non-aging creep tensor function of CEM II hydrates
$\mathbb{J}_{hyd}^{*,II}$	Laplace–Carson-transformed universal isochoric creep tensor function of CEM II hydrates
J_{con}	Uniaxial non-aging creep function of concrete
$J_{con}^* = J_{1111}$	Laplace–Carson-transformed uniaxial creep function of concrete
$\mathbb{J}_d$	Creep rate tensor function
J_d	Uniaxial creep rate function
k_{blt}	Bulk modulus of basalt
k_{cli}	Bulk modulus of clinker
k_{con}	Bulk modulus of concrete
k_{dbs}	Bulk modulus of diabase
k_{dol}	Bulk modulus of dolomite
k_{grt}	Bulk modulus of granite
k_{hyd}	Bulk modulus of hydrates
k_{lim}	Bulk modulus of limestone
k_{por}	Bulk modulus of pores
k_{qzt}	Bulk modulus of quarzite
k_{slg}	Bulk modulus of slag
ℓ	Characteristic length of a RVE
m_{cli}	Mass of clinker
m_{reac}	Mass of reactants
$m_{\mathrm{H_2O}}$	Mass of water
m_{lim}	Mass of limestone
m_{hyd}	Mass of hydrates
$m_{\mathrm{H_2O}}/m_{cli}$	Initial water-to-clinker mass ratio
m_{lim}/m_{cli}	Initial limestone-to-clinker mass ratio
m_{slg}/m_{cli}	Initial slag-to-clinker mass ratio
m_{slg}/m_{lim}	Initial slag-to-limestone mass ratio
N_D	Number of readings from the creep test of Dummer et al. [30]
N_K	Number of readings from the creep test at KAT3
$\mathbb{P}_{sph}$, $\mathbb{P}_{cyl}$	Fourth-order Hill tensor for spherical and cylindrical inclusions
$\mathbb{P}_{sph}^*$, $\mathbb{P}_{cyl}^*$	Laplace–Carson-transformed fourth-order Hill tensor for spherical and cylindrical inclusions
p	Variable in the LC space
Q	Activation energy of bulk water
R	Universal gas constant
$\mathbb{R}$	Relaxation tensor function
$\mathbb{R}^*$	Laplace–Carson-transformed relaxation tensor function
$\mathbb{R}_{con}^*$	Laplace–Carson-transformed relaxation tensor function of concrete
$\mathbb{R}_{cp}^*$	Laplace–Carson-transformed relaxation tensor function of cement paste
$\mathbb{R}_{hyd}^{*,II}$	Laplace–Carson-transformed relaxation tensor function of CEM II hydrates
$\mathbb{R}_{hf}^*$	Laplace–Carson-transformed relaxation tensor function of hydrate foam
$\mathcal{R}$	Minimum root-mean-squared error
$\mathcal{R}_W$	Weighted mean of absolute values of relative errors
S	Uniaxial creep compliance
S_{exp}	Uniaxial creep compliance from experiments
s	Dimensionless parameter
T	Temperature
t	Recording time
t_{eq}	Temperature-dependent equivalent concrete age
t_n	Time of readings during the creep test
t_0	Start of the creep test
t_{ref}	Reference time
t_{tst}	Transition time instant
Δt_i	Number of days where the temperature T prevails
V_{cp}	Volume of cement paste
V_{cli}	Volume of clinker
V_{slg}	Volume of slag
V_{lim}	Volume of limestone
$V_{\mathrm{H_2O}}$	Volume of water
β	Power-law creep exponent
ε_{exp}	Basic creep strains from experiments
$\boldsymbol{\varepsilon}$	Strain tensor
$\boldsymbol{\varepsilon}^*$	Laplace–Carson-transformed strain tensor
$\dot{\boldsymbol{\varepsilon}}$	Strain rate tensor
Γ	Gamma function
μ_{blt}	Shear modulus of basalt
μ_{cli}	Shear modulus of clinker
μ_{con}	Shear modulus of concrete
μ_{dbs}	Shear modulus of diabase
μ_{dol}	Shear modulus of dolomite
μ_{grt}	Shear modulus of granite
μ_{hyd}	Shear modulus of hydrates
μ_{lim}	Shear modulus of limestone
μ_{por}	Shear modulus of pores
μ_{qzt}	Shear modulus of quarzite
μ_{slg}	Shear modulus of slag
$\mu_{c,hyd}$	Shear creep modulus of CEM I hydrates at $\varphi = 100\%$ and $T = 20°\mathrm{C}$
$\tilde{\mu}_{c,hyd}^{II}$	Shear creep modulus of CEM II hydrates at $\varphi = 100\%$ and $T = 20°\mathrm{C}$
$\mu_{c,hyd}^{II}$	Shear creep modulus of CEM II hydrates
ν_{con}	Poisson's ratio of concrete
$\rho_{cp}^{con}(\xi = 0)$	Initial apparent mass density of cement paste in concrete
$\rho_{cemII}^{con}(\xi = 0)$	Initial apparent mass density of CEM II in concrete
$\rho_{\mathrm{H_2O}}^{con}(\xi = 0)$	Initial apparent mass density of water in concrete
ρ_{cp}	Mass density of cement paste
ρ_{cli}	Mass density of clinker
ρ_{lim}	Mass density of limestone
ρ_{slg}	Mass density of slag
$\rho_{\mathrm{H_2O}}$	Mass density of water
ρ_{reac}	Mass density of reactants
$\boldsymbol{\sigma}$	Stress tensor

$\boldsymbol{\sigma}^*$	Laplace–Carson-transformed stress tensor
$\dot{\boldsymbol{\sigma}}$	Stress rate tensor
σ_{exp}	Compressive normal stress from experiments
τ	Time instant of loading
ϕ, θ	Polar angles
φ	Relative humidity
ξ	Hydration degree
$\dot{\xi}$	Rate of the hydration degree
$\mathbf{1}$	Second-order identity tensor

Data availability

Data will be made available on request.

References

[1] J.M. Paris, J.G. Roessler, C.C. Ferraro, H.D. DeFord, T.G. Townsend, A review of waste products utilized as supplements to Portland cement in concrete, J. Clean. Prod. 121 (2016) 1–18.

[2] M. Amran, G. Murali, N.H.A. Khalid, R. Fediuk, T. Ozbakkaloglu, Y.H. Lee, S. Haruna, Y.Y. Lee, Slag uses in making an ecofriendly and sustainable concrete: A review, Constr. Build. Mater. 272 (2021) 121942.

[3] EN 197-1, Cement - Part 1: Composition, specifications and conformity criteria for common cements, 2011.

[4] K.L. Scrivener, V.M. John, E.M. Gartner, Eco-efficient cements: Potential economically viable solutions for a low-CO2 cement-based materials industry, Cem. Concr. Res. 114 (2018) 2–26.

[5] B. Lothenbach, K. Scrivener, R. Hooton, Supplementary cementitious materials, Cem. Concr. Res. 41 (12) (2011) 1244–1256.

[6] R. Khatri, V. Sirivivatnanon, W. Gross, Effect of different supplementary cementitious materials on mechanical properties of high performance concrete, Cem. Concr. Res. 25 (1) (1995) 209–220.

[7] M. Shariq, J. Prasad, H. Abbas, Creep and drying shrinkage of concrete containing GGBFS, Cem. Concr. Compos. 68 (2016) 35–45.

[8] Y. Gan, M. Vandamme, H. Zhang, Y. Chen, E. Schlangen, K. van Breugel, B. Šavija, Micro-cantilever testing on the short-term creep behaviour of cement paste at micro-scale, Cem. Concr. Res. 134 (2020) 106105.

[9] M. Königsberger, M. Irfan-ul Hassan, B. Pichler, C. Hellmich, Downscaling based identification of nonaging power-law creep of cement hydrates, J. Eng. Mech. 142 (12) (2016) 04016106.

[10] P. Yu, Y. Duan, E. Chen, S. Tang, A. Hanif, Y. Fan, Microstructure-based homogenization method for early-age creep of cement paste, Constr. Build. Mater. 188 (2018) 1193–1206.

[11] M. Königsberger, T. Honório, J. Sanahuja, B. Delsaute, B.L. Pichler, Homogenization of nonaging basic creep of cementitious materials: A multiscale modeling benchmark, Constr. Build. Mater. 290 (2021) 123144.

[12] S. Liang, Y. Wei, New insights into creep and creep recovery of hardened cement paste at micro scale, Constr. Build. Mater. 248 (2020) 118724.

[13] N. Laws, R. McLaughlin, Self-consistent estimates for the viscoelastic creep compliances of composite materials, Proc. R. Soc. A 359 (1697) (1978) 251–273.

[14] S. Beurthey, A. Zaoui, Structural morphology and relaxation spectra of viscoelastic heterogeneous materials, Eur. J. Mech. A Solids 19 (1) (2000) 1–16.

[15] A. Zaoui, Continuum micromechanics: survey, J. Eng. Mech. 128 (8) (2002) 808–816.

[16] S. Baweja, G.J. Dvorak, Z.P. Bažant, Triaxial composite model for basic creep of concrete, J. Eng. Mech. 124 (9) (1998) 959–965.

[17] J. Sanahuja, Effective behaviour of ageing linear viscoelastic composites: Homogenization approach, Int. J. Solids Struct. 50 (19) (2013) 2846–2856.

[18] F. Lavergne, K. Sab, J. Sanahuja, M. Bornert, C. Toulemonde, Investigation of the effect of aggregates' morphology on concrete creep properties by numerical simulations, Cem. Concr. Res. 71 (2015) 14–28.

[19] F. Lavergne, K. Sab, J. Sanahuja, M. Bornert, C. Toulemonde, Homogenization schemes for aging linear viscoelastic matrix-inclusion composite materials with elongated inclusions, Int. J. Solids Struct. 80 (2016) 545–560.

[20] J. Sanahuja, S. Huang, Mean-field homogenization of time-evolving microstructures with viscoelastic phases: application to a simplified micromechanical model of hydrating cement paste, J. Nanomechanics Micromechanics 7 (1) (2017) 04016011.

[21] S. Scheiner, C. Hellmich, Continuum microviscoelasticity model for aging basic creep of early-age concrete, J. Eng. Mech. 135 (4) (2009) 307–323.

[22] S. Ullah, B. Pichler, S. Scheiner, C. Hellmich, Shell-specific interpolation of measured 3D displacements, for micromechanics-based rapid safety assessment of shotcrete tunnels, Comput. Model. Eng. Sci. (CMES) 57 (3) (2010) 279.

[23] S. Ullah, B. Pichler, S. Scheiner, C. Hellmich, Influence of shotcrete composition on load-level estimation in NATM-tunnel shells: Micromechanics-based sensitivity analyses, Int. J. Numer. Anal. Methods Geomech. 36 (9) (2012) 1151–1180.

[24] R. Scharf, B. Pichler, R. Heissenberger, B. Moritz, C. Hellmich, Data-driven analytical mechanics of aging viscoelastic shotcrete tunnel shells, Acta Mech. 233 (8) (2022) 2989–3019.

[25] R. Scharf, M. Sorgner, S. Scheiner, B. Pichler, C. Hellmich, Viscoelasticity of hydrating shotcrete as key to realistic tunnel shell stress assessment with the New Austrian Tunneling Method, Mech. Adv. Mater. Struct. (2024) 1–16.

[26] B. Pichler, C. Hellmich, Upscaling quasi-brittle strength of cement paste and mortar: A multi-scale engineering mechanics model, Cem. Concr. Res. 41 (5) (2011) 467–476.

[27] M. Königsberger, M. Hlobil, B. Delsaute, S. Staquet, C. Hellmich, B. Pichler, Hydrate failure in ITZ governs concrete strength: A micro-to-macro validated engineering mechanics model, Cem. Concr. Res. 103 (2018) 77–94.

[28] A. Aili, M. Vandamme, J.-M. Torrenti, B. Masson, J. Sanahuja, Time evolutions of non-aging viscoelastic Poisson's ratio of concrete and implications for creep of CSH, Cem. Concr. Res. 90 (2016) 144–161.

[29] A. Razgordanisharahi, M. Sorgner, T. Pilgerstorfer, B. Moritz, C. Hellmich, B.L.A. Pichler, Realistic long-term stress levels in a deep segmented tunnel lining, from hereditary mechanics-informed evaluation of strain measurements, Tunn. Undergr. Space Technol. 145 (2024) 105602.

[30] A. Dummer, S. Smaniotto, G. Hofstetter, Experimental and numerical study on nonlinear basic and drying creep of normal strength concrete under uniaxial compression, Constr. Build. Mater. 362 (2023) 129726.

[31] P. Acker, Micromechanical analysis of creep and shrinkage mechanisms, in: F.-J. Ulm, Z.P. Bažant, F.H. Wittmann (Eds.), Creep, Shrinkage and Durability Mechanics of Concrete and Other Quasi-Brittle Materials, 6th International Conference CONCREEP@MIT, Elsevier, Amsterdam, 2001, pp. 15–26.

[32] G. Constantinides, F.-J. Ulm, The effect of two types of CSH on the elasticity of cement-based materials: Results from nanoindentation and micromechanical modeling, Cem. Concr. Res. 34 (1) (2004) 67–80.

[33] O. Bernard, F.-J. Ulm, E. Lemarchand, A multiscale micromechanics-hydration model for the early-age elastic properties of cement-based materials, Cem. Concr. Res. 33 (9) (2003) 1293–1309.

[34] C. Hu, Z. Li, A review on the mechanical properties of cement-based materials measured by nanoindentation, Constr. Build. Mater. 90 (2015) 80–90.

[35] V. Jagsch, P. Kuttke, O. Lahayne, L. Zelaya-Lainez, S. Scheiner, C. Hellmich, Multiscale and multitechnique investigation of the elasticity of grooved rail steel, Constr. Build. Mater. 238 (2020) 117768.

[36] M. Königsberger, L. Zelaya-Lainez, O. Lahayne, B.L. Pichler, C. Hellmich, Nanoindentation-probed Oliver-Pharr half-spaces in alkali-activated slag-fly ash pastes: Multimethod identification of microelasticity and hardness, Mech. Adv. Mater. Struct. 29 (26) (2022) 4878–4889.

[37] R. Helmuth, D. Turk, Elastic moduli of hardened portland cement and tricalcium silicate pastes: Effect of porosity, in: Symposium on Structure of Portland Cement Paste and Concrete, Vol. 90, Highway Research Board, Washington, DC, 1966, pp. 135–144.

[38] V.Z. Zadeh, C.P. Bobko, Nanoscale mechanical properties of concrete containing blast furnace slag and fly ash before and after thermal damage, Cem. Concr. Compos. 37 (2013) 215–221.

[39] A.C.A. Muller, Characterization of Porosity & CSH in Cement Pastes by ^{1}H NMR, Technical Report, Epfl, 2014.

[40] M. Königsberger, J. Carette, Validated hydration model for slag-blended cement based on calorimetry measurements, Cem. Concr. Res. 128 (2020) 105950.

[41] H. Wang, H. Mang, Y. Yuan, B.L. Pichler, Multiscale thermoelastic analysis of the thermal expansion coefficient and of microscopic thermal stresses of mature concrete, Materials 12 (17) (2019) 2689.

[42] ÖNORM B 4710-3, Concrete - Specification, performance, production, use and conformity - Part 3: National application of testing standards for concrete and its source materials, 2023.

[43] I. Fischer, B. Pichler, E. Lach, C. Terner, E. Barraud, F. Britz, Compressive strength of cement paste as a function of loading rate: Experiments and engineering mechanics analysis, Cem. Concr. Res. 58 (2014) 186–200.

[44] M.F. Ruiz, A. Muttoni, P.G. Gambarova, Relationship between nonlinear creep and cracking of concrete under uniaxial compression, J. Adv. Concr. Technol. 5 (3) (2007) 383–393.

[45] Z. Jiang, Z. Sun, P. Wang, Autogenous relative humidity change and autogenous shrinkage of high-performance cement pastes, Cem. Concr. Res. 35 (8) (2005) 1539–1545.

[46] Z. Hashin, Analysis of composite materials—A survey, J. Appl. Mech. 50 (3) (1983) 481–505.

[47] W.J. Drugan, J.R. Willis, A micromechanics-based nonlocal constitutive equation and estimates of representative volume element size for elastic composites, J. Mech. Phys. Solids 44 (4) (1996) 497–524.

[48] P.M.J. Godinho, M. Jajcinovic, L. Wagner, V. Vass, W.J. Fischer, T.K. Bader, U. Hirn, W. Bauer, J. Eberhardsteiner, C. Hellmich, A continuum micromechanics approach to the elasticity and strength of planar fiber networks: Theory and application to paper sheets, Eur. J. Mech. A Solids 75 (2019) 516–531.
[49] A. Shahsavari, R. Picu, Size effect on mechanical behavior of random fiber networks, Int. J. Solids Struct. 50 (20–21) (2013) 3332–3338.
[50] C. Kohlhauser, C. Hellmich, Ultrasonic contact pulse transmission for elastic wave velocity and stiffness determination: Influence of specimen geometry and porosity, Eng. Struct. 47 (2013) 115–133.
[51] N. Jiménez Segura, B.L. Pichler, C. Hellmich, Stress average rule derived through the principle of virtual power, ZAMM-J. Appl. Math. Mech./Z. Angew. Math. Mech. 102 (9) (2022) e202200091.
[52] A. Fritsch, C. Hellmich, 'Universal'microstructural patterns in cortical and trabecular, extracellular and extravascular bone materials: micromechanics-based prediction of anisotropic elasticity, J. Theoret. Biol. 244 (4) (2007) 597–620.
[53] B. Pichler, C. Hellmich, J. Eberhardsteiner, Spherical and acicular representation of hydrates in a micromechanical model for cement paste: prediction of early-age elasticity and strength, Acta Mech. 203 (3–4) (2009) 137–162.
[54] M. Königsberger, B. Pichler, C. Hellmich, Multiscale poro-elasticity of densifying calcium-silicate hydrates in cement paste: An experimentally validated continuum micromechanics approach, Internat. J. Engrg. Sci. 147 (2020) 103196.
[55] E. Binder, M. Königsberger, R. Díaz Flores, H.A. Mang, C. Hellmich, B.L. Pichler, Thermally activated viscoelasticity of cement paste: minute-long creep tests and micromechanical link to molecular properties, Cem. Concr. Res. 163 (2023) 107014.
[56] R. Hill, A self-consistent mechanics of composite materials, J. Mech. Phys. Solids 13 (4) (1965) 213–222.
[57] C. Hellmich, H. Mang, Shotcrete elasticity revisited in the framework of continuum micromechanics: From submicron to meter level, J. Mater. Civ. Eng. 17 (3) (2005) 246–256.
[58] J.D. Eshelby, The determination of the elastic field of an ellipsoidal inclusion, and related problems, Proc. R. Soc. Lond. Ser. A Math. Phys. Eng. Sci. 241 (1226) (1957) 376–396.
[59] A. Fritsch, L. Dormieux, C. Hellmich, Porous polycrystals built up by uniformly and axisymmetrically oriented needles: homogenization of elastic properties, Comptes Rendus Mécanique 334 (3) (2006) 151–157.
[60] T. Mori, K. Tanaka, Average stress in matrix and average elastic energy of materials with misfitting inclusions, Acta Metall. 21 (5) (1973) 571–574.
[61] N.J. Segura, B.L. Pichler, C. Hellmich, Concentration tensors preserving elastic symmetry of multiphase composites, Mech. Mater. 178 (2023) 104555.
[62] L. Ježo, M. Palou, J. Kozánková, T. Ifka, Determination of activation effect of Ca (OH) 2 upon the hydration of BFS and related heat by isothermal calorimeter, J. Therm. Anal. Calorim. 101 (2) (2010) 585–593.
[63] T.C. Powers, T. Brownyard, Studies of the Physical Properties of Hardened Portland Cement Paste, vol. 22, Research Laboratories of the Portland Cement Association Bulletin, 1948, pp. 101–992.
[64] T.J. Ahrens, T.J. Ahrens, Mineral Physics & Crystallography: A Handbook of Physical Constants, vol. 2, American Geophysical Union Washington, DC, 1995.
[65] C. Hua, P. Acker, A. Ehrlacher, Analyses and models of the autogenous shrinkage of hardening cement paste: I. Modelling at macroscopic scale, Cem. Concr. Res. 25 (7) (1995) 1457–1468.
[66] P. Acker, Swelling, shrinkage and creep: a mechanical approach to cement hydration, Mater. Struct. 37 (2004) 237–243.
[67] H. Le Chatelier, Sur les changements de volume qui accompagnent le durcissement des ciments, in: Bulletin Societe De L'encouragement Pour L'industrie Nationale, Vol. 5, 1900.
[68] F.-J. Ulm, O. Coussy, Strength growth as chemo-plastic hardening in early age concrete, J. Eng. Mech. 122 (12) (1996) 1123–1132.
[69] C. Hellmich, F.-J. Ulm, H.A. Mang, Consistent linearization in finite element analysis of coupled chemo-thermal problems with exo-or endothermal reactions, Comput. Mech. 24 (4) (1999) 238–244.
[70] P. Karte, M. Hlobil, R. Reihsner, W. Dörner, O. Lahayne, J. Eberhardsteiner, B. Pichler, Unloading-based stiffness characterisation of cement pastes during the second, third and fourth day after production, Strain 51 (2) (2015) 156–169.
[71] International Federation for Structural Concrete, FIB Model Code for Concrete Structures 2010, International Federation for Structural Concrete: Lausanne, Switzerland, 2013.
[72] M. Irfan-ul Hassan, B. Pichler, R. Reihsner, C. Hellmich, Elastic and creep properties of young cement paste, as determined from hourly repeated minute-long quasi-static tests, Cem. Concr. Res. 82 (2016) 36–49.
[73] B. Delsaute, C. Boulay, S. Staquet, Creep testing of concrete since setting time by means of permanent and repeated minute-long loadings, Cem. Concr. Compos. 73 (2016) 75–88.
[74] M. Irfan-ul Hassan, M. Königsberger, R. Reihsner, C. Hellmich, B. Pichler, How water-aggregate interactions affect concrete creep: Multiscale analysis, J. Nanomechanics Micromechanics 7 (4) (2017) 04017019.
[75] Q. Zhang, R. Le Roy, M. Vandamme, B. Zuber, Long-term creep properties of cementitious materials: Comparing microindentation testing with macroscopic uniaxial compressive testing, Cem. Concr. Res. 58 (2014) 89–98.
[76] J. Frech-Baronet, L. Sorelli, Z. Chen, A closer look at the temperature effect on basic creep of cement pastes by microindentation, Constr. Build. Mater. 258 (2020) 119455.
[77] P. Acker, F.-J. Ulm, Creep and shrinkage of concrete: physical origins and practical measurements, Nucl. Eng. Des. 203 (2–3) (2001) 143–158.
[78] L. Boltzmann, Zur theorie der elastischen Nachwirkung, Ann. Phys., Lpz. 241 (11) (1878) 430–432.
[79] M.E. Gurtin, E. Sternberg, et al., On the linear theory of viscoelasticity, Arch. Ration. Mech. Anal. 11 (1) (1962) 291–356.
[80] H. Markovitz, Boltzmann and the beginnings of linear viscoelasticity, Trans. Soc. Rheol. 21 (3) (1977) 381–398.
[81] F. Schwarzl, L. Struik, Analysis of relaxation measurements, Adv. Mol. Relax. Process. 1 (3) (1968) 201–255.
[82] C. Donolato, Analytical and numerical inversion of the Laplace–Carson transform by a differential method, Comput. Phys. Comm. 145 (2) (2002) 298–309.
[83] W. Read Jr., Stress analysis for compressible viscoelastic materials, J. Appl. Phys. 21 (7) (1950) 671–674.
[84] L. Yuan, J. Qiu, Z. Guo, S. Zhang, X. Wan, X. Sun, Microscale and macroscale strength behaviors of blast furnace slag-cement based materials: Modeling and analysis, Constr. Build. Mater. 376 (2023) 131016.
[85] A.C. Muller, K.L. Scrivener, A.M. Gajewicz, P.J. McDonald, Densification of C–S–H measured by 1H NMR relaxometry, J. Phys. Chem. C 117 (1) (2013) 403–412.
[86] A. Muller, K. Scrivener, A. Gajewicz, P. McDonald, Use of bench-top NMR to measure the density, composition and desorption isotherm of C–S–H in cement paste, Microporous Mesop. Mater. 178 (2013) 99–103.
[87] A.M. Gajewicz-Jaromin, P.J. McDonald, A.C. Muller, K.L. Scrivener, Influence of curing temperature on cement paste microstructure measured by 1H NMR relaxometry, Cem. Concr. Res. 122 (2019) 147–156.
[88] S. Joseph, M. Mutti, T. Ohkubo, I. Maruyama, Ö. Cizer, Microstructural analysis of cement paste blended with blast furnace slag using 1H NMR relaxometry, Cem. Concr. Compos. 146 (2024) 105377.
[89] M. Königsberger, C. Hellmich, B. Pichler, Densification of CSH is mainly driven by available precipitation space, as quantified through an analytical cement hydration model based on NMR data, Cem. Concr. Res. 88 (2016) 170–183.
[90] N.J. Segura, B.L. Pichler, C. Hellmich, Mix-, storage- and temperature-invariant precipitation characteristics in white cement paste, expressed through an NMR-based analytical model, Cem. Concr. Res. 172 (2023) 107237.
[91] H. Wang, C. Hellmich, Y. Yuan, H. Mang, B. Pichler, May reversible water uptake/release by hydrates explain the thermal expansion of cement paste?—Arguments from an inverse multiscale analysis, Cem. Concr. Res. 113 (2018) 13–26.
[92] M. Wyrzykowski, P.J. McDonald, K.L. Scrivener, P. Lura, Water redistribution within the microstructure of cementitious materials due to temperature changes studied with 1H NMR, J. Phys. Chem. C 121 (50) (2017) 27950–27962.
[93] M. Wyrzykowski, A.M. Gajewicz-Jaromin, P.J. McDonald, D.J. Dunstan, K.L. Scrivener, P. Lura, Water redistribution–microdiffusion in cement paste under mechanical loading evidenced by 1H NMR, J. Phys. Chem. C 123 (26) (2019) 16153–16163.
[94] I. Pane, W. Hansen, Investigation of blended cement hydration by isothermal calorimetry and thermal analysis, Cem. Concr. Res. 35 (6) (2005) 1155–1164.
[95] H. Kada-Benameur, E. Wirquin, B. Duthoit, Determination of apparent activation energy of concrete by isothermal calorimetry, Cem. Concr. Res. 30 (2) (2000) 301–305.
[96] O. Linderoth, L. Wadsö, D. Jansen, Long-term cement hydration studies with isothermal calorimetry, Cem. Concr. Res. 141 (2021) 106344.
[97] M. Ausweger, E. Binder, O. Lahayne, R. Reihsner, G. Maier, M. Peyerl, B. Pichler, Early-age evolution of strength, stiffness, and non-aging creep of concretes: Experimental characterization and correlation analysis, Materials 12 (2) (2019) 207.
[98] C. Hellmich, F.-J. Ulm, H.A. Mang, Multisurface chemoplasticity. I: Material model for shotcrete, J. Eng. Mech. 125 (6) (1999) 692–701.
[99] C. Hellmich, H.A. Mang, F.-J. Ulm, Hybrid method for quantification of stress states in shotcrete tunnel shells: combination of 3D in situ displacement measurements and thermochemoplastic material law, Comput. Struct. 79 (22–25) (2001) 2103–2115.
[100] L. Charpin, Y. Le Pape, É. Coustabeau, É. Toppani, G. Heinfling, C. Le Bellego, B. Masson, J. Montalvo, A. Courtois, J. Sanahuja, et al., A 12 year EDF study of concrete creep under uniaxial and biaxial loading, Cem. Concr. Res. 103 (2018) 140–159.
[101] A. Luxmoore, S. Sekisambu, A simple triaxial rig for studying the creep of concrete at elevated temperatures, Strain 12 (3) (1976) 107–112.
[102] Z.P. Bažant, S. Prasannan, High-temperature triaxial torsional creep tests of concrete at various hygral conditions, Nucl. Eng. Des. 94 (2) (1986) 137–151.